CATÓLICA
ESCOLA SUPERIOR DE BIOTECNOLOGIA
PORTO

DETERGENT-FREE SUPERCRITICAL CARBON DIOXIDE – ASSISTED PROTOCOL FOR THE PRODUCTION OF SUSTAINABLE AND HIGHLY PRESERVED DECELLULARIZED PORCINE MENISCUS FOR ORTHOPEDIC APPLICATIONS

by
Chou I Ho

July 2025

CATÓLICA
ESCOLA SUPERIOR DE BIOTECNOLOGIA
PORTO

DETERGENT-FREE SUPERCRITICAL CARBON DIOXIDE – ASSISTED PROTOCOL FOR THE PRODUCTION OF SUSTAINABLE AND HIGHLY PRESERVED DECELLULARIZED PORCINE MENISCUS FOR ORTHOPEDIC APPLICATIONS

Thesis presented to *Escola Superior de Biotecnologia* of the *Universidade Católica Portuguesa* to fulfill the requirements of a Master of Science degree in Biomedical Engineering

by
Chou I Ho

Place: Universidade Católica Portuguesa
Supervisor: Ph.D. João Bebiano Costa
Co-supervisor: Prof. Ana Leite Oliveira

July 2025

Abstract

The development of biologically functional scaffolds for meniscal applications using the extracellular matrix (ECM) as a source has been shown to be a promising alternative to tissue engineered strategies. Therefore, there is a need to achieve efficient decellularization strategies that can effectively eliminate cellular and genetic materials to minimize immunogenic responses, while maximally preserving the ECM to support subsequent cellular activities essential for tissue regeneration. Conventional decellularization methods generally rely on harsh chemicals that are associated with ECM damage, cytotoxic residues, and prolonged processing times, compromising tissue integrity and biocompatibility. These limitations have driven the exploration of supercritical carbon dioxide ($scCO_2$)—a green and minimally invasive technology—as an alternative decellularization agent to develop faster, more cost-effective, and environmentally sustainable approaches. This study evaluated a series of $scCO_2$-assisted decellularization protocols, where operational parameters including number of cycles, depressurization speed, applied pressures, exposure time, co-solvent application, as well as washing strategies with distinct solvents, washing modes, and physical interventions were tested. Decellularization efficiency was assessed via quantification of residual dsDNA. Moreover, ECM preservation was assessed using biochemical assays for glycosaminoglycans (GAGs), soluble collagen, and insoluble collagen, alongside Fourier transform infrared spectroscopy with attenuated total reflectance (FTIR-ATR) and the corresponding chemometric analysis. These assessments for ECM preservation were further conducted after sterilization applying $scCO_2$ with the additive NovaKill^{TM}, a mixture comprising peracetic acid (PAA) and hydrogen peroxide (H_2O_2). The $scCO_2$-assisted protocol—employing nine cycles at 160 bars and integrating freeze-thaw, direct sonication with an ultrasonic processor, and lyophilization—achieved the highest decellularization efficiency, with residual dsDNA of 88.74 ± 10.25 ng/mg of dry sample. Additionally, biochemical assay results demonstrated great preservation of ECM, with only minimal degradation suggested by spectroscopic analysis. Following sterilization, no significant differences were observed in the ECM quantification results and FTIR spectral analysis, indicating an optimal ECM preservation. These findings highlight the potential of generating decellularized ECM (dECM) by $scCO_2$-assisted approaches as a promising candidate for advanced meniscal regenerative applications.

Keywords: Orthopedic application; Meniscus regeneration; Porcine meniscus decellularization; Supercritical carbon dioxide; Extracellular matrix preservation

Resumo

O desenvolvimento de scaffolds biologicamente funcionais para aplicações meniscais, utilizando a matriz extracelular (ECM) como fonte, tem-se revelado uma alternativa promissora às estratégias de engenharia tecidular. Assim, torna-se necessário desenvolver estratégias de descelularização eficientes que consigam eliminar de forma eficaz os materiais celulares e genéticos, minimizando as respostas imunogénicas e, ao mesmo tempo, preservar ao máximo a ECM, de modo a apoiar as atividades celulares subsequentes essenciais para a regeneração tecidular. Os métodos convencionais de descelularização baseiam-se geralmente na utilização de agentes químicos agressivos, associados à degradação da ECM, à presença de resíduos citotóxicos e a tempos de processamento prolongados, comprometendo a integridade e biocompatibilidade do tecido. Estas limitações têm impulsionado a exploração do dióxido de carbono supercrítico ($scCO_2$)—uma tecnologia verde e minimamente invasiva—como agente alternativo de descelularização, visando o desenvolvimento de abordagens mais rápidas, económicas e sustentáveis do ponto de vista ambiental. Neste estudo, foi avaliada uma série de protocolos de descelularização assistidos por $scCO_2$, nos quais foram testados parâmetros operacionais, incluindo o número de ciclos, a velocidade de despressurização, as pressões aplicadas, o tempo de exposição, a utilização de co-solventes, bem como estratégias de lavagem com diferentes solventes, modos de lavagem e intervenções físicas. A eficiência de descelularização foi avaliada através da quantificação de DNA de dupla hélice (dsDNA) residual. A preservação da ECM foi analisada por meio de ensaios bioquímicos para quantificação de glicosaminoglicanos (GAGs), colagénio solúvel e colagénio insolúvel, em paralelo com espectroscopia de infravermelho por transformada de Fourier com reflectância total atenuada (FTIR-ATR) e respetiva análise quimiométrica. Estas avaliações foram também realizadas após esterilização com $scCO_2$ e o aditivo NovaKillTM, uma mistura composta por ácido peracético (PAA) e peróxido de hidrogénio (H_2O_2). O protocolo assistido por $scCO_2$—envolvendo nove ciclos a 160 bar e integrando ciclos de congelação-descongelação, sonicação direta com processador ultrassónico e liofilização—demonstrou a maior eficiência de descelularização, com um conteúdo residual de dsDNA de 88,74 ± 10,25 ng/mg de amostra seca. Adicionalmente, os resultados dos ensaios bioquímicos demonstraram uma preservação significativa da ECM, com apenas degradações mínimas sugeridas pela análise espectroscópica. Após esterilização, não foram observadas diferenças significativas nos resultados da quantificação da ECM nem na análise espectral por FTIR, indicando uma preservação ótima da matriz. Estes resultados destacam o potencial da geração de ECM descelularizada (dECM)

através de abordagens assistidas por $scCO_2$ como uma estratégia promissora para aplicações avançadas em regeneração meniscal.

Palavra-chave: Aplicação ortopédica; Regeneração meniscal; Descelularização de menisco porcino; Dióxido de carbono supercrítico; Preservação da matriz extracelular

Acknowledgments

Firstly, I would like to express my gratitude to my supervisors, Ph.D. João Bebiano Costa, for unwavering support when I was blue, insightful guidance for me to develop critical mindset, and continuous trust and encouragement that I appreciate the most, and Prof. Ana Leite Oliveira for accepting me in this research group and providing advice and support throughout the journey of this work. Their expertise and patience have been significant not only in shaping the direction of this thesis, but also in my growth as a researcher. It has been a privilege to work under their supervision.

Secondly, I would like to thank all my lab colleagues for their generous help, collaboration, and patience—especially during moments when I was under pressure or in a rush. I would also like to thank my friends outside academy, specifically Best, for being my listener when I was out of my mind.

Thirdly, I would like to thank my family members, especially my mother, for being supportive and encouraging when I was crying through the Facetime with her, and being extremely patient with me to call me over and over again when I was not in a healthy mindset.

Lastly, a little thanks to myself for not giving up and being gradual resilience when facing challenges.

Contents

List of Figures

List of Tables

List of abbreviations

ECM – Extracellular matrix
GAG(s) – Glycosaminoglycan(s)
AC – Articular cartilage
OA – Osteoarthritis
PCL – Polycaprolactone
PUR – Polyurethane
PCU – Polycarbonate urethane
RGD – Arginine-glycine-aspartic acid
PLGA – Poly(lactic-co-glycolic acid)
dsDNA – Double-stranded DNA
DNA – Deoxyribonucleic acid
SDS – Sodium dodecyl sulfate
SDC – Sodium deoxycholate
DNase – Deoxyribonuclease
RNase – Ribonuclease
EDTA – Ethylenediaminetetraacetic acid
UPW – Ultrapure water
CO_2 – Carbon dioxide
$scCO_2$ – Supercritical carbon dioxide
dECM – Decellularized ECM
EtOH – Ethanol
PAA – Peracetic acid
H_2O_2 – Hydrogen peroxide
NaOH – Sodium hydroxide
PBS – Phosphate-buffered saline
FTIR – Fourier transform infrared
PV(s) – Protocol version(s)
CLO – Chloramphenicol
P – Pressure
T – Temperature
t – Time
DMSO – Dimethyl sulfoxide
PCA – Principal component analysis
SNV – Standard normal variate
Savgol – Savitzky-Golay
NaCl – Sodium chloride

HCl – Hydrogen chloride

SD – Standard deviation

PC1 – First principal component

PC2 – Second principal component

1. Introduction

1.1. Meniscus

The menisci are crescent-shaped fibrocartilaginous structures located on the medial and lateral aspects of the tibial plateau within the knee joint (Figure 1) (Wu *et al.*, 2021; Bian *et al.*, 2024). Macroscopically, the meniscus exhibits a wedge-like profile, with thickness decreasing from the peripheral edge toward the inner margin. This geometry enhances congruency between the tibial plateau and femoral condyles, forming a load-distributing cushion essential for joint function (Wu *et al.*, 2021). The lateral meniscus is more mobile due to its thinner and more flexible attachment to the joint capsule, while the medial meniscus is more firmly anchored, particularly at its midpoint where it is stabilized by the medial collateral ligament connecting the femur to the tibia (Bian *et al.*, 2024).

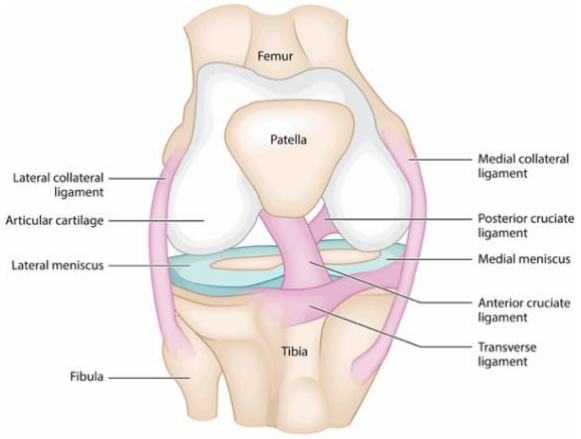

Figure 1 – Schematic representation of the human knee joint, illustrating the anatomical positioning of the medial and lateral menisci in relation to the surrounding osseous structures and principal ligamentous attachments (Murphy *et al.*, 2019).

Anatomically, the meniscus is subdivided into three zones based on vascularization and innervation (Figure 2). The outer third, known as the "red zone", is well vascularized and innervated, thus possessing a higher capacity for healing. The inner third, termed the "white zone", is avascular and aneural, significantly limiting its regenerative potential. Between these regions lies the "red-white zone", which demonstrates intermediate vascularity and partial healing capability (Bian *et al.*, 2024; Murphy *et al.*, 2019; Kwon *et al.*, 2019).

The meniscal extracellular matrix (ECM) composition and cellular phenotype vary spatially, contributing to its hierarchical architecture. The peripheral zone, namely the red zone and the adjacent red-white zone, predominantly comprises type I collagen with low glycosaminoglycans (GAGs) content, providing tensile strength and efficient load transmission, especially in the circumferential direction. In contrast, the inner zone, principally related to the

white zone, is rich in type II collagen and GAGs, contributing to viscoelastic properties and enhanced compressive stiffness (Wu *et al.*, 2021; Bian *et al.*, 2024; Murphy *et al.*, 2019; Berni *et al.*, 2021). These structural and compositional differences underlie the critical role of meniscus in knee biomechanics, including joint stabilization, load distribution, lubrication, and shock absorption between the femur and tibia (Wu *et al.*, 2021; Bian *et al.*, 2024; Porzucek *et al.*, 2024). Regarding cellular distribution, oval-shaped fibrochondrocytes, spindle-shaped fibroblast-like cells, and endothelial cells are primarily located in the outer zone of the meniscus, often connected through elongated cellular extensions. Conversely, round chondrocyte-like cells are predominantly found within the inner zone. Additionally, meniscal surface comprises superficial cells exhibiting flattened, fibroblast-like morphologies (Karjalainen *et al.*, 2024; Bian *et al.*, 2024; Berni *et al.*, 2021; Suzuki *et al.*, 2020). The porcine meniscus contains a substantial number of resident cells, with cell density varying markedly across different zones of the tissue. Specifically, the outer region demonstrates a higher cellular density, associated with elevated expression of type I collagen, indicative of its fibrous composition. In contrast, the inner region is characterized by a lower cell density and thereby increased expression of type II collagen and aggrecan, mirroring the biochemical profile of articular cartilage (AC) (Jacob *et al.*, 2019; Chen *et al.*, 2018; Gonzalez-Leon *et al.*, 2022). This zonal variation in cellular and ECM composition underscores the functional heterogeneity of meniscal tissue (Wu *et al.*, 2021).

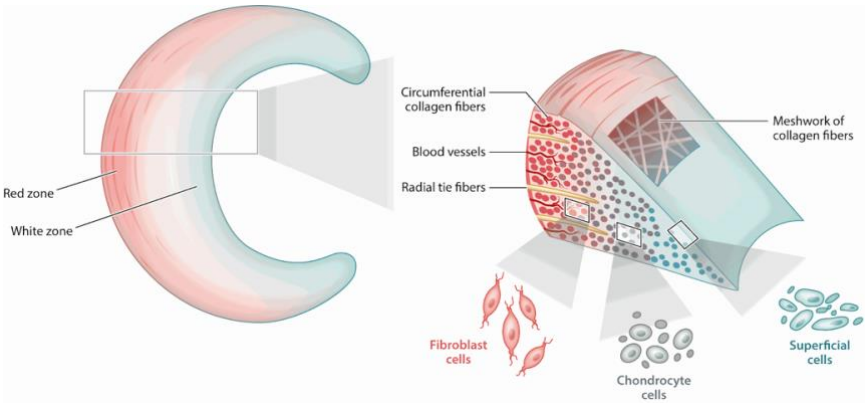

Figure 2 – Structural organization of the meniscus, highlighting regional differences in vascularization, collagen network, and cellular distribution (Murphy *et al.*, 2019).

1.2. Knee Meniscus injuries

Given the essential role of the knee joint in nearly all daily movements, meniscal injuries are relatively common, with an estimated annual incidence of 66 to 70 cases per 100,000 individuals (Bian *et al.*, 2024). These injuries are frequently associated with factors such as increased body mass, high-impact athletic activities—of which approximately 63.8%

necessitate surgical intervention—and age-related degeneration, a growing concern in the context of global population aging (Bian *et al.*, 2024; Porzucek *et al.*, 2024).

Meniscal tears are generally classified into two major categories based on their orientation: vertical tears, which include longitudinal, radial, and oblique types; and horizontal tears, which encompass flap and cleavage lesions (Figure 3) (Bian *et al.*, 2024; Kwon *et al.*, 2019). Clinically, meniscal injuries typically manifest as joint pain, swelling, mechanical instability, and restricted range of motion. Structural damage to the meniscus can compromise normal load distribution across the knee joint, leading to altered stress transmission to the articular cartilage (AC) of the femur and tibia. Over time, such biomechanical disruption significantly increases the risk of osteoarthritis (OA), with approximately 50% of patients with chronic meniscal tears developing OA or related degenerative cartilage conditions within 10 to 20 years (Wu *et al.*, 2021; Bian *et al.*, 2024). In addition, injuries involving the avascular inner region of the meniscus are particularly challenging to treat due to the inherently limited regenerative capacity of the region (Porzucek *et al.*, 2024; He *et al.*, 2020). The limited intrinsic healing capacity of the meniscus presents a significant challenge to strategies focused on its preservation and functional restoration. Consequently, meniscal injuries—and their progression to degenerative joint diseases—remain a major clinical challenge in orthopedic practice and represent a substantial burden on healthcare systems worldwide (Bian *et al.*, 2024; He *et al.*, 2020).

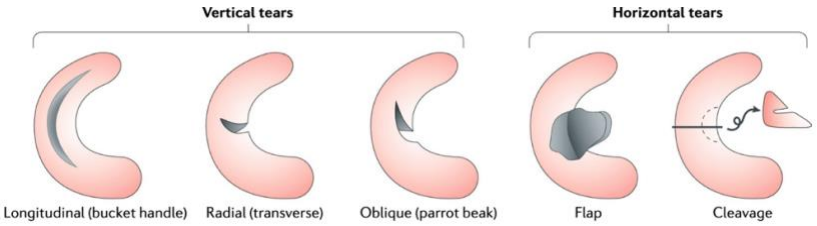

Figure 3 – Classification of meniscal tear patterns, illustrating common defect types including vertical and horizontal lesions (Kwon *et al.*, 2019).

1.3. Clinically available treatments for knee injuries

Current clinical management of meniscal injuries, intended at mitigating their progression toward degenerative joint disorders such as OA, comprises both conservative and surgical interventions.

Conservative treatment, generally reserved for horizontal cleavage tears and minor longitudinal tears, primarily aims to alleviate symptoms rather than promote tissue repair. The widely recommended RICE protocol—Rest, Ice, Compression, and Elevation—is typically employed in the initial stages following minor injuries to reduce inflammation and pain (Fischer *et al.*, 2021). Analgesics may also be prescribed for pain management. However, inappropriate or

prolonged use poses a risk of drug dependence (Lim *et al.*, 2022). Importantly, conservative methods do not facilitate tissue regeneration and are ineffective for long-term functional restoration of the meniscus. Therefore, transition to surgical treatment is considered when conservative treatments fail after four to six weeks, especially in cases of persistent pain, swelling, or mechanical symptoms like locking or instability (Bian *et al.*, 2024). Concerning surgical interventions, they remain the mainstay for more severe or unresponsive cases, namely vertical tears, specifically when displaced in the inner avascular zone. Partial or total meniscectomy has historically been one of the most frequently performed procedures, involving the removal of damaged meniscal tissue. Despite providing temporary symptom relief, meniscectomy significantly alters knee joint biomechanics by increasing contact stress on the tibial plateau, thereby accelerating cartilage degradation. Long-term outcomes are concerning, with nearly half of patients developing OA within 10 to 20 years post-meniscectomy (Bian *et al.*, 2024; Porzucek *et al.*, 2024).

Meniscal repair techniques have gained increasing clinical interest due to their potential to preserve native meniscal function. However, their success is largely dependent on factors such as tear location, size, and the degree of vascularization. Healing is often incomplete in avascular regions, and the likelihood of surgical failure rises with the severity of tissue damage (Bian *et al.*, 2024; Yeo *et al.*, 2019). Meniscal allograft transplantation has also been adopted as a means of restoring knee function and alleviating pain. Although this approach has demonstrated promising results, its broader application is constrained by challenges such as limited donor availability, potential for disease transmission, immunological complications, and concerns regarding long-term graft viability (Bian *et al.*, 2024; He *et al.*, 2020). Autologous grafts derived from tissues such as the infrapatellar fat pad, quadriceps tendon, or Achilles tendon have been explored in tissue augmentation approaches, offering favorable biocompatibility but lacking the mechanical and structural characteristics and architecture of native meniscus tissue (He *et al.*, 2020).

Meniscal implants have recently emerged as a viable alternative in clinical research and early-phase applications. Currently, four types of meniscal scaffolds are under investigation or in use. For segmental meniscal defects with minimal cartilage damage, the collagen-based meniscus implant (CMI), composed of type I collagen and GAGs derived from bovine Achilles tendon, is commercially available in the United States and has shown potential in pain reduction and functional improvement with a low failure rate. In Europe, the polyurethane-based scaffold Actifit®—a blend of polycarprolactone (PCL) and polyurethane (PUR)—has demonstrated improved mechanical performance and favorable clinical outcomes for patients post-partial

meniscectomy over a period of four years. For total meniscus replacement, the NUsurface® prosthesis, composed of polycarbonate urethane (PCU) reinforced with PUR, is undergoing Food and Drug Administration (FDA) clinical trials. It mimics the physical and biomechanical properties of the native meniscus and has shown encouraging preclinical results (Bian *et al.*, 2024; Kwon et al., 2019; Bian *et al.*, 2025; Otsuki *et al.*, 2024). Despite these advances, meniscal implants face notable limitations that hinder their widespread adoption. These include the inability to promote intrinsic meniscal regeneration, unclear efficacy in preventing OA progression, difficulties in accurate arthroscopic placement, and technical challenges related to fixation and suturing during implantation procedures (Kwon et al., 2019). As such, while current treatments offer varying degrees of symptom management and functional restoration, the development of an ideal therapeutic solution for meniscal injury remains an ongoing clinical and research challenge.

1.4. Meniscus tissue engineering

Given the limitations and technical challenges associated with current clinical treatments for meniscal injuries, ongoing research in meniscus tissue engineering seeks to develop advanced implant strategies. By integrating principles of meniscal biology, materials science, and engineering, tissue-engineered scaffolds aim to achieve optimal biocompatibility, appropriate mechanical properties, and the capacity to regenerate fully functional meniscal tissue, ultimately reducing the risk of OA development (Bian *et al.*, 2024; Jian *et al.*, 2021).

Meniscus tissue engineering typically involves scaffolds composed of either natural or synthetic polymers, combined with various cell sources such as stem cells or fibrochondrocytes to facilitate tissue regeneration (Wu *et al.*, 2021; Bian *et al.*, 2024). Natural polymers—including collagen, silk fibroin, and alginate—offer inherent biocompatibility, minimal disruption to host homeostasis, enzymatic biodegradability, and favorable remodeling by host cells. Additionally, bioactive motifs such as the arginine-glycine-aspartic acid (RGD) sequence enhance cell adhesion, while their structural versatility allows adaptation to complex meniscal geometries (Bian *et al.*, 2024; Abpeikar *et al.*, 2022). However, these materials often lack sufficient mechanical strength required for load-bearing applications. Moreover, most studies compare these scaffolds only to untreated defects rather than established clinical standards such as meniscal repair or autografts, limiting their demonstrated clinical relevance (Bian *et al.*, 2024). Synthetic polymers—some of which are currently employed in clinical applications, including PCL, PUR, and poly(lactic-co-glycolic acid) (PLGA)—provide suitable mechanical properties (Li *et al.*, 2021). However, they exhibit limited capacity to promote tissue regeneration and

remodeling (Guo *et al.*, 2021). Moreover, they may be associated with postoperative complications including poor implant fixation, increased AC damage, and a complete torn posterior horn extension (Bian *et al.*, 2024).

To overcome these drawbacks, composite scaffolds integrating both natural and synthetic polymers have been developed to balance regenerative potential with mechanical durability (Bian *et al.*, 2024). For instance, Kim *et al.* (2021) incorporated polyethylene oxide (PEO) into fibrin scaffolds, which were subsequently evaluated in a rabbit partial meniscectomy model. This composite scaffold promoted enhanced meniscal tissue regeneration accompanied by improved biomechanical properties. Despite these advances, challenges persist regarding scaffold structural integrity, biological integration, degradation kinetics, customization for patient-specific defects, and clinical translation (Bian *et al.*, 2024; Kwon *et al.*, 2019; Vadodaria *et al.*, 2019). As an alternative, xenografts derived from decellularized biological tissues have gained increasing interest. These biological scaffolds provide a tissue-specific microenvironment conducive to regeneration by preserving native ECM architecture, offering suitable mechanical performance and inductive cues essential for functional repair and remodeling (Wu *et al.*, 2021; Porzucek *et al.* 2024). For instance, Wu et al. (2015) reported that a decellularized procine meniscus-derived ECM hydrogel exhibited a fibrous morphology with tunable compressive properties and initial modulus through variations in ECM concentration, thereby facilitating cellular proliferation within two weeks and promoting rapid cellular infiltration both *in vitro* and *in vivo*.

1.4.1. Biological scaffolds – Xenogeneic meniscus sources

Xenogeneic meniscal tissues have emerged as promising alternatives as raw materials for the development of tissue-engineered scaffolds, largely due to their anatomical, mechanical, and ECM similarities to the human meniscus, as well as their ready availability (He *et al.*, 2020). Mammalian menisci generally share a consistent semilunar shape regardless of donor species, size, or locomotion style. Consequently, animals such as dogs, pigs, sheep, goats, cows, and rabbits have been widely employed as models in meniscal research (Takroni *et al.*, 2016). Among these, porcine, ovine, and bovine menisci have received particular attention due to their anatomical and key biomechanical resemblances to the human menisci (Table 1).

Table 1 – Key properties of human, porcine, ovine, and bovine meniscus (Gonzalez-Leon *et al.*, 2022; Fischenich *et al.*, 2017; Murphy *et al.*, 2019; Di Giancamillo *et al.*, 2014)

	Structural features	Biochemical composition	Mechanical properties
Human	Thicker posterior region 5–7 mm peripheral height 33–40 mm anteroposterior length	Collagen: 22% GAG: 0.8%	Circumferential: 100–300 MPa Radial: 1–4 Mpa Compressive: 100–150 kPa
Pig (Porcine)	Smaller than human 6.4–8.4 mm peripheral height 23.2–24.8 anteroposterior length	Collagen: 23.9–31.3% GAG: 1.20–2.57%	Circumferential: 78.4–116.2 MPa Radial: 2.5–10.9 Mpa Compressive: 157–287 kPa
Sheep (Ovine)	Smaller than human but larger than pig Similar zonal structure	Collagen: similar to human GAG: higher in anterior horn	Compressive: 450 kPa (higher than human)
Cow (Bovine)	Larger and thick than human More pronounced zonal structure	Collagen: 80% GAG: lower than human	Compressive: 100–150 kPa

Although ovine meniscus demonstrates closer anatomical and biomechanical similarity to the human meniscus, porcine meniscus is often preferred owing to its higher availability, lower cost (especially in *ex vivo* applications), and well-documented compatibility with decellularization protocols (Chen *et al.*, 2024; Mazy *et al.*, 2024). Furthermore, in anatomical aspect, the porcine meniscus shows notable parallels with human tissue, including comparable size, cartilage thickness, and weight (Han *et al.*, 2020). Moreover, porcine menisci exhibit a collagen fiber arrangement that closely mirrors that of humans, characterized by a predominantly circumferential orientation. This contrasts with the columnar collagen architecture commonly found in smaller laboratory animals such as rats, rabbits, and dogs (Han *et al.*, 2020). Given these anatomical, physiological, and serum biochemical similarities to humans, porcine meniscus remains a principal xenogeneic source for decellularization studies in meniscal tissue engineering.

1.5. Decellularization of biological tissues: porcine meniscus ECM

Decellularization is a critical technique for the development of biocompatible biological scaffolds, aimed at removing cellular and intracellular components while preserving the native ECM structure and signaling elements. This process seeks to eliminate nuclear, cellular, and antigenic materials that could provoke immune rejection upon transplantation, while maintaining the biochemical and biophysical integrity of the ECM, including vascular and neural architectures when possible (Golebiowska *et al.*, 2024). Preservation of the intrinsic ECM composition is essential as it provides structural support and biochemical cues that regulate key cellular functions such as adhesion, migration, proliferation, and differentiation (McCrary *et al.*, 2020). In general, the effectiveness of decellularization is typically assessed by established criteria: residual double-stranded deoxyribonucleic acid (dsDNA) content below 50 ng per mg of dry tissue, DNA fragment sizes under 200 base pairs, and the absence of visible nuclear remnants (Dehghani *et al.*, 2024).

Currently, several decellularized tissue products have reached clinical application for regenerative therapies, including porcine dermis (Conexa™, Tornier, The Netherlands), porcine small intestinal submucosa (Oasis® and Surgisis®, Cook Biotech Inc., USA), and porcine urinary bladder matrix (MatriStem®, Acell Inc., USA) (McCrary *et al.*, 2020; Parmaksiz *et al.*, 2016). However, decellularized meniscal tissues have yet to achieve widespread clinical adoption. Notably, a decellularized porcine meniscus xenograft (dCELL® by Tissue Regenix, UK) commenced patient recruitment in July 2015, but its clinical trial was suspended in November 2018 (McCrary *et al.*, 2020). Accordingly, decellularized biological scaffolds hold significant scientific and clinical promise as natural bio-instructive materials capable of recreating tissue-specific microenvironments, thereby facilitating the regulation of cellular behavior and promoting tissue regeneration (McCrary *et al.*, 2020; Golebiowska *et al.*, 2024).

1.5.1. Conventional decellularization process

Decellularization of biological tissues has been extensively explored using chemical, physical, and enzymatic methods. Chemical agents are frequently employed to solubilize cellular membranes, dissociate nucleic acids, and disrupt lipid-protein interactions. Detergents, classified as ionic (e.g., sodium dodecyl sulfate (SDS), sodium deoxycholate (SDC)), non-ionic (e.g., Triton X-100), and zwitterionic (e.g., CHAPS), are amphipathic molecules that disrupt protein-protein, lipid-protein, and lipid-lipid interactions (Golebiowska *et al.*, 2024). Hypotonic solutions, such as 10 mM Tris HCl, have a lower solute concentraion than the intracellular environment, leading to osmotic swelling. Conversly, hypertonic solutions, like 50 mM Tris HCl, exert higher osmotic pressure, leading to cellular shrinkage. Alternating between these conditions imposes osmotic stress that filitates cell membrane disruption (McCrary *et al.*, 2020). Additionally, acids and bases facilitate DNA dissociation and cytoplasmic solubilization, while organic solvents such as alcohols and acetone promote dehydration leading to cell lysis (Golebiowska *et al.*, 2024). Physical techniques include freeze-thaw cycles, pressure gradients, mechanical agitation, and sonication, which physically disrupt cell membranes and enhance removal of cellular debris from the ECM (McCrary *et al.*, 2020). Enzymatic methods target specific components: nucleases (deoxyribonuclease (DNase), ribonuclease (RNase)) degrade nucleic acids by cleaving phosphodiester bonds, and trypsin cleaves peptide bonds at arginine and lysine residues, often combined with chelating agents like ethylenediaminetetraacetic acid (EDTA) to dissociate cells by binding divalent cations at adhesion sites (McCrary *et al.*, 2020; Golebiowska *et al.*, 2024).

These conventional methods have been widely applied for porcine meniscus decellularization. Ding *et al.* (2022) utilized cyclic freeze-thaw grinding combined with DNase treatment to prepare decellularized ECM particles. Porcine menisci were sliced, subjected to repeated freeze-thaw cycles at -80°C for 2 hours, ground at RT, and incubated with DNase (20 KU/ml) in magnesium chloride for 2 hours with gentle agitation. Similarly, Li *et al.* (2023) developed region-specific decellularized porcine menisci by treating sliced tissues in 0.25% trypsin-EDTA at 37°C for 24 hours with agitation, followed by incubation in 1% SDS and 1% Triton X-100 for 48 hours and extensive rinsing with water for one week.

While these conventional protocols effectively reduce DNA content below 50 ng/mg dry weight, they pose significant limitations in terms of biocompatibility, mechanical integrity, immune response, scalability, and clinical translation (White *et al.*, 2017). Additionally, residual chemicals such as SDS and Triton X-100 can provoke inflammatory responses in vivo if not completely removed, limiting their clinical approval in tissue engineering (Fernández-Pérez *et al.*, 2019). Extensive washing with large volumes of ultrapure water (UPW)—typically several cycles over several hours or even days—is required to mitigate this issue, rendering the process time-consuming (Cebotari *et al.*, 2010). Moreover, prolonged exposure to harsh reagents often leads to excessive degradation of the ECM, compromising mechanical properties and the ability of the scaffold to support cellular activities and withstand physiological loads (Mendibil *et al.*, 2020). Consequently, these drawbacks underscore the need for faster and cost-effective decellularization strategies.

1.5.2. Supercritical carbon dioxide ($scCO_2$)-assisted decellularization

A supercritical fluid is defined as a substance at a temperature and pressure above its critical point (Tc and Pc, respectively), where it no longer exists as a distinct liquid or gas but instead exhibits intermediate properties of both phases (Topuz *et al.*, 2020). Carbon dioxide (CO_2) reaches its supercritical state under relatively mild conditions—above 31.1 °C and 73.8 bar—making it particularly attractive for biomedical applications (Figure 4). In this state, supercritical CO_2 combines both gas-like diffusivity and viscosity with liquid-like density and solvating capacity, enabling effective penetration into complex biological matrices (Kim *et al.*, 2021).

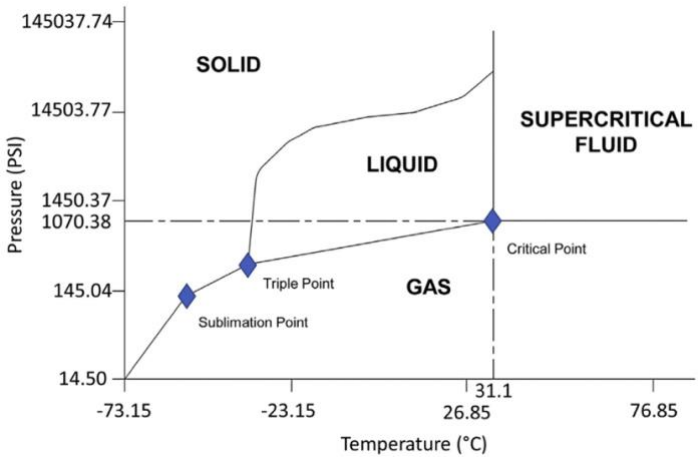

Figure 4 – Phase diagram illustrating the supercritical region of CO_2 (Topuz *et al.*, 2020).

Supercritical CO_2 has been widely employed across various biomedical and industrial applications due to its unique physicochemical properties—high tissue permeability, chemical inertness, non-toxicity, non-flammability, and cost-effectiveness (Kim *et al.*, 2021). In biomedical contexts, $scCO_2$ has been effectively utilized for the sterilization of medical devices such as implants, surgical instruments, and drug delivery systems (Okolie *et al.*, 2022). When combined with co-solvents like hydrogen peroxide or peracetic acid, $scCO_2$ demonstrates potent bactericidal and virucidal activity, serving as an innovative alternative to traditional sterilization methods such as ethylene oxide (Topuz *et al.*, 2020). Through rapid depressurization, $scCO_2$ disrupts microbial structures, enabling the inactivation of a wide range of microorganisms, including bacterial spores and fungi (Topuz *et al.*, 2020; Bernhardt *et al.*, 2015). In addition to sterilization, $scCO_2$ serves as a standard method for drying applications, particularly in aerogel production, where it contributes to off-the-shelf accessibility when paired with its sterilization capability (Bento *et al.*, 2022). Beyond the biomedical field, $scCO_2$ is also extensively applied in food processing for microbial inactivation and compound extraction, as well as in pharmaceutical manufacturing to improve formulations and drug impregnation (Montalbán *et al.*, 2022).

Given these advantageous characteristics, $scCO_2$ has gained significant interest for its application in tissue engineering. Under high-pressure conditions, $scCO_2$ permeates biological matrices and induces cellular rupture; upon depressurization, it transitions to a gaseous state, facilitating the evaporation and effective removal of cellular debris without leaving behind toxic solvent residues (Kim *et al.*, 2021). Furthermore, when used with co-solvents, $scCO_2$ promotes tissue dehydration, enabling extended shelf-life (Porzucek *et al.*, 2024). Moreover, its operation under mild critical conditions helps preserve the native structure of proteins within the ECM (Topuz *et al.*, 2020). These combined features make $scCO_2$ a compelling alternative to

conventional decellularization approaches, potentially offering accelerated processing, reduced reliance on cytotoxic detergents and organic solvents, and the production of relatively sterile and structurally preserved acellular tissues.

1.6. State of the art

The production of highly preserved decellularized ECM (dECM) has become a foundational strategy in biomedical applications, providing a biological source with native biochemical and structural cues essential for guiding cellular behavior to facilitate further tissue repair and remodeling. Nevertheless, traditional decellularization protocols, particularly with the applications of chemical detergents and enzymatic treatments, often demonstrate limitations, including ECM damage, cytotoxic residue retention, extended processing time, high costs, and environmental burden. In response to these shortcomings, the scientific community is actively exploring alternative approaches in decellularization, offering faster, more cost-effective, and environmentally sustainable solutions, while still ensuring the structural and functional preservation of dECM. Among these, scCO2 has emerged as a particularly promising candidate. $scCO_2$-assisted decellularization has been applied to a variety of biological tissues, demonstrating promising outcomes. For instance, porcine peripheral nerve tissues were decellularized using $scCO_2$ at pressures ranging from 200 to 300 bar for 3 hours, and ethanol (EtOH) was used as a co-solvent. This protocol resulted in a significant reduction of dsDNA content, along with decreased expression of cellular surface markers MHC I and II. Importantly, essential ECM components were preserved, contributing to enhanced peripheral nerve regeneration efficacy (Choi *et al.*, 2024). Ozudogru *et al.* (2024) utilized supercritical CO_2-based decellularization to process bovine spinal cord meninges for hydrogel fabrication. Compared to conventional detergent-based methods, this approach achieved superior preservation of extracellular matrix components and mechanical integrity, while the resulting hydrogel demonstrated high cell viability and biocompatibility.

Regarding porcine meniscus, $scCO_2$-assisted decellularization remains relatively underexplored. Nevertheless, a recent study by Porzucek *et al.* (2024) introduced a method wherein minced meniscal tissues underwent a sequence of pretreatments—aqueous extraction, lactic acid extraction, cryomilling, lyophilization, and enzymatic hydrolysis with pepsin—prior to exposure to $scCO_2$. The $scCO_2$ treatment was performed in batch mode for 20 hours at 300 bar and 40°C, using EtOH as a co-solvent. This approach only yielded a 37.7% reduction relative to native tissue, while preserving 92.9% of collagen and 59.9% of GAGs. Additionally, a more prolonged $scCO_2$-based protocol spanning 22 days has been developed, involving six

treatment cycles at approximately 310 bar and 37°C. This was supplemented by physical, chemical, and enzymatic treatments, including freeze-thaw, hypotonic and hypertonic agitation, and sodium hydroxide (NaOH) incubation. The protocol achieved a progressive reduction in dsDNA, reaching 50.46 ± 6.34 ng in the fifth cycle and 42.53 ± 4.18 ng in the sixth cycle (Zihna *et al.*, 2025).

1.7. Objectives

The primary objective of this study is to develop a highly preserved ECM derived from porcine meniscus, suitable for applications such as tissue transplantation, injectable hydrogels, or bioink formulations in regenerative medicine. To achieve this, $scCO_2$ is explored as a central decellularization strategy due to its potential advantages, including promising preservation of ECM component and integrity, rapid processing, cost-efficiency, non-toxicity, and environmental sustainability. Additionally, although the application of $scCO_2$ is emerging as a promising strategy for porcine meniscus decellularization, current protocols often require the use of chemical agents—such as enzymes and chelators—and involve prolonged, labor-intensive procedures to achieve effective decellularization.

To address these challenges, this study aims to develop a chemically mild and time-efficient supercritical CO_2-based decellularization protocol for porcine meniscus that avoids the use of detergents, enzymes, and chelating agents. The goal is to maximize the preservation of the ECM, thereby maintaining its biochemical and biophysical properties to support the regulation of cellular behavior in future regenerative applications. The decellularization approach was systematically developed across four protocol iterations, evaluating the modifications related to sample architectures and operational parameters in the $scCO_2$ treatment. To enhance decellularization efficiency, intermediate washing steps were conducted, with distinct solvents and physical interventions being tested. Afterwards, $scCO_2$-based sterilization was performed on the samples resulted from the establishment of the most optimized protocol.

Decellularization efficiency was evaluated through DNA quantification across all developed protocols. Following the elimination of suboptimal protocols, ECM preservation, particularly collagen and GAGs, was assessed using quantitative analyses, and Fourier-transform infrared (FTIR) spectroscopy was employed to examine the biochemical integrity and conformational stability of key matrix components. These assessments of ECM preservation were also conducted after $scCO_2$ sterilization to evaluate its influences in decellularized matrices.

2. Methodology

2.1. Decellularization of porcine meniscus

2.1.1. Sample segmentation and preliminary cleaning

Porcine meniscal tissues (Figure 5A) were obtained with the support of local butchers and the Faculty of Medicine of the University of Porto. Upon collection, surrounding adipose tissue was meticulously removed from the meniscal samples and rinsed with phosphate-buffered saline (PBS) (Figure 5B). Subsequently, the menisci were sectioned into two distinct architectures for downstream analyses: (1) cubic segments of approximately 1 cm^3 (CUBE) (Figure 5C), and (2) vertically oriented slices (SLICE) (Figure 5D). These two architectures were used to investigate morphological effects on decellularization efficiency. All segmented samples were stored at -20°C until further processing.

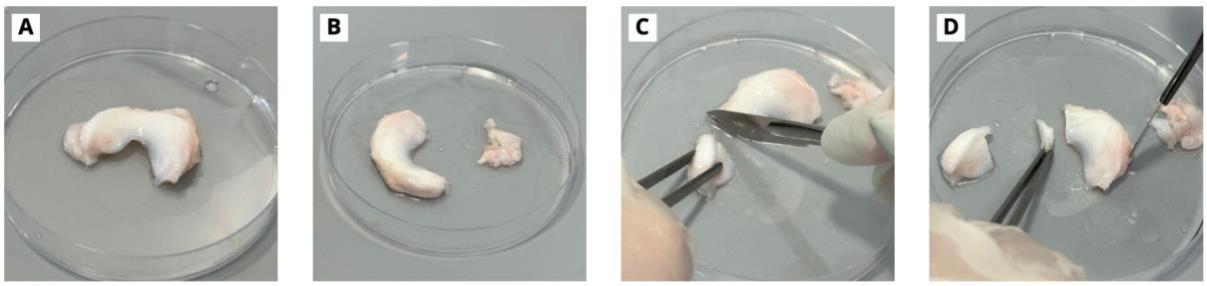

Figure 5 – Meniscal sample (A) in native tissue, (B) after removal of adipose tissue, (C) segmented in cube, and (D) segmented in slice.

2.1.2. $scCO_2$ reactor setup and operational parameters

All $scCO_2$-assisted decellularization procedures were conducted using the NovaGenesis $scCO_2$ reactor (NovaSterilis™) (Figure 6A), equipped with a 600 mL vessel (Figure 6B). Mechanical stirring within the vessel was employed to enhance the homogeneity of the $scCO_2$ phase.

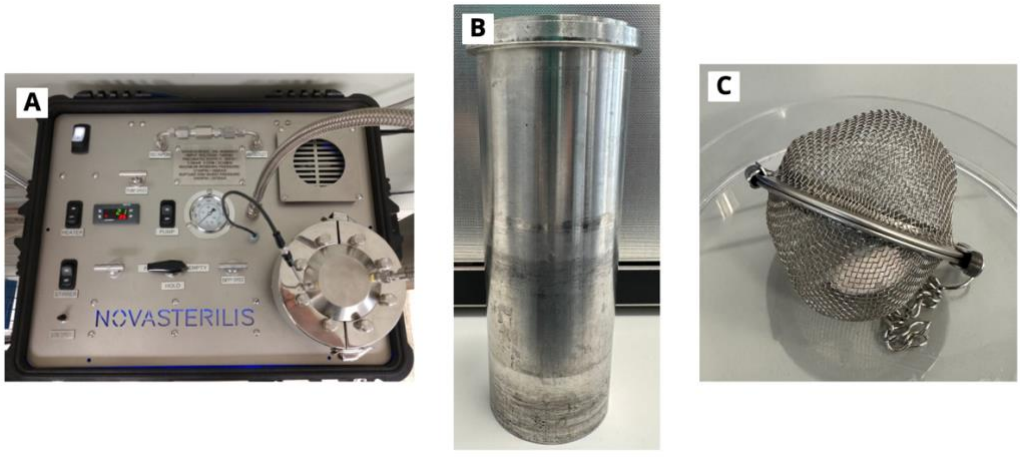

Figure 6 – (A) NovaGenesis $scCO_2$ reactor equipped with (B) a 600 mL vessel. (C) Meniscal sample in the metallic container.

In all protocols, $scCO_2$ treatment was conducted in batch mode, with each batch consisting of one complete cycle of pressurization, heating, exposure to $scCO_2$, and depressurization. Prior to sample loading, the reactor vessel was pre-cleaned with EtOH. Afterwards, meniscal tissues were placed inside a metallic container (Figure 6C) to prevent displacement during $scCO_2$ exposure and depressurization. The vessel was then sealed using mechanical torque to ensure an airtight environment and prevent leakage throughout the process. Notably, due to equipment limitations, a mandatory cooling interval of at least three hours was required between successive $scCO_2$ cycles to restore the operational capacity of the $scCO_2$ pump.

Operational parameters varied among protocol versions. Two different pressures were tested: 120 and 160 bar. In all versions, the process temperature was maintained between 35–40 °C during the cycles. Moreover, two different $scCO_2$ exposure times (1 hour and 2 hours) were tested. Furthermore, EtOH was employed as a co-solvent by adding 120 mL to the base of the vessel prior to sample loading, ensuring no direct contact between the tissue and the solvent. Two different concentrations were applied: 70% and 96% (v/v). Furthermore, two modes of depressurization were tested: rapid depressurization, where pressure was released instantaneously, and slow depressurization, where pressure was gradually released, lasting approximately 7 minutes.

2.1.3. Intermediate washing steps

The washing steps were performed using UPW and PBS under orbital agitation. Each washing phase lasted approximately three hours. Firstly, two distinct modes of washing were tested: (1) static mode (Static) – the washing solution was manually replaced; and (2) in continuous mode (Continuous) – a peristaltic pumps operating at a flow rate of 7 mL/min was used to replace the washing solution, aiming to minimize manual handling and maintain fluid exchange.

2.1.3.1 Physical methods

Several physical approaches were investigated to enhance decellularization efficiency, which were implemented during the washing steps between successive supercritical CO_2 cycles. These methods included: (1) bath sonication – performed using an ultrasonic bath; (2) direct sonication – an ultrasonic processor (Sigma-Aldrich, St. Louis, MO, USA; 130 W, input 220 V) was used, where the sonicator probe was directly immersed in the washing solution containing the meniscal tissues (approximate distance of 3 cm between the probe and the tissue). Two intensities were used in direct sonication: 40% amplitude with intermittent 30-second pauses (Direct sonication – 40%), and another at a higher intensity of 60% amplitude applied continuously (Direct sonication – 60%); (3) freeze-thaw – a freeze and a thaw step were applied

in cyclic mode (5 cycles, involved alternating freezing in liquid nitrogen for approximately 1 minute, followed by thawing in a 37°C water bath for 5 minutes); (4) and lyophilization – samples were rapidly frozen in liquid nitrogen for at least 5 minutes to ensure complete solidification and freeze-dried overnight; Additional orbital shaking and vortexing were applied during the washing steps.

2.1.3.2 Detergent treatment

Detergent treatment, contained 0.5% SDC and 1 M DMSO, was incorporated into the washing steps between $scCO_2$ cycles in selected protocol version. This detergent-based washing step was also supplemented with the aforementioned physical interventions.

2.1.4. Development of $scCO_2$-assisted decellularization protocols

Four versions of porcine meniscal decellularization protocols were systematically developed, each iteratively refined based on the outcomes of preceding approaches.

For each protocol version, all native meniscal tissues were initially rinsed with PBS for 10 minutes on an orbital shaker. Control samples were subsequently stored at –80 °C until lyophilization alongside their respective treated samples. The protocol development strategy was based on cyclic $scCO_2$ treatment, wherein each cycle involved exposing the meniscal samples to supercritical CO_2 within the reactor, followed by intermediate washing steps incorporating physical interventions (Table 2).

Table 2 – Schematic representation of the seven developed protocols for $scCO_2$-assisted porcine meniscus decellularization.

		PV1	PV2	PV3	PV4
Number of cyclic $scCO_2$ treatment		**1 or 2**	**9**	**9**	**9**
Tested sample architectures		**CUBE**	**CUBE**	**CUBE**	**CUBE / SLICE**
Operational parameters in the $scCO_2$ treatment	**Pressure (bar)**	120	120	120	160
	Duration per cycle (hour)	1	1	1	1 or 2
	Co-solvent	----	----	----	Ethanol
	Depressurization	Rapid	Slow	Slow	Slow with only the 2º cycle being rapid
Intermediate washing steps	**Washing mode**	Static / Continuous	Static	Static	Static
	Washing solvents	UPW	UPW	UPW following PBS / Detergent	UPW following PBS
	Involved physical interventions	----	Bath sonication	Freeze-thaw Direct sonication – 40% Lyophilization	Freeze-thaw Direct sonication – 60% Lyophilization

Notably, in the decellularization protocols incorporating detergent treatment—specifically PV3—the samples were subjected to additional rinsing with UPW for two consecutive days to facilitate detergent removal. Following the completion of all decellularization procedures, both

treated and non-treated (control) samples were rinsed with PBS for 30 minutes. Subsequently, the samples were frozen overnight at -80°C, which were then lyophilized for a minimum of two days prior to the employment of following characterization analyses. A detailed overview of each developed protocol, including time schedules, is provided in the supplementary appendices.

2.2. Sterilization of porcine meniscus

For sterilization, a $scCO_2$-based procedure was performed using meniscal samples processed under PV7. A sterile gauze pre-soaked with 1.5 mL of NovaKill™ (NovaSterilis™)—a proprietary mixture of peracetic acid (PAA) and hydrogen peroxide (H_2O_2)—was placed at the base of the reactor vessel. The samples were then loaded into the vessel, with 1.25 mL of UPW applied to the inner wall to maintain adequate humidity throughout the process. The $scCO_2$ reactor was operated at 110 bar and approximately 35 °C for 3 hours, followed by a controlled slow depressurization. To remove residual NovaKill reagent from the tissue matrix, an additional $scCO_2$ cycle was conducted at 120 bar and below 40 °C for 1 hour. Following this treatment, the samples were placed in a sterile flow chamber for 48 hours to facilitate complete evaporation of any remaining chemical residues.

2.3. Fourier transform infrared (FTIR) spectroscopic analysis

2.3.1. Spectral acquisition

FTIR technique, particularly under the ATR (Attenuated Total Reflectance) sampling methodology, was employed. FTIR-ATR applies the total internal reflection property of a high-refractive-index trapezoidal crystal, generating an evanescent wave when an infrared beam interacts with it (Bieberle-Hütter *et al.*, 2021). It was performed on lyophilized meniscal samples to eliminate moisture-related spectral interference. Spectral acquisition was carried out using the PerkinElmer Spectrum 10 software (PerkinElmer Inc., Waltham, MA, USA), with all measurement parameters standardized according to the specifications of the instrument (Table 3). Spectra were recorded over a wavenumber range of 4000 cm^{-1} to 600 cm^{-1} on the x-axis, representing the infrared radiation frequency transmitted through the sample. The y-axis corresponded to the percentage transmittance, indicating the proportion of infrared light passing through the tissue. Spectral resolution was set to 4 cm^{-1}, with data points collected at 2 cm^{-1} intervals across the defined range. Each measurement comprised 32 co-added scans to enhance the signal-to-noise ratio by averaging.

Prior to sample loading, the FTIR crystal platform was thoroughly cleaned with EtOH, followed by a background scan to subtract atmospheric and instrumental noise. The meniscal sample was

carefully positioned to fully cover the crystal surface. A screw mechanism was employed to ensure uniform pressure distribution between the sample and the crystal, facilitating consistent infrared light interaction for reproducible spectral acquisition. Moreover, five replicate spectra were collected per sample to ensure data reliability. The raw spectral data were subsequently exported to MATLAB R2019a (MathWorks Inc., Natick, MA, USA) for advanced processing and analysis.

Table 3 – FTIR spectra settings.

Category	Parameter	Value
Settings	Abscissa Units	Wavenumber
	Ordinate Units	%T
	Start (cm^{-1})	4000
	End (cm^{-1})	600
Scan Settings	Resolution (cm^{-1})	4
	Data Interval (cm^{-1})	2
	Scan Type	Sample
	Accumulations	32 scans

2.3.2. Chemometric analysis

Data analysis techniques were applied to extract meaningful information from the raw FTIR spectra and to elucidate underlying differences between samples. Initially, the spectra were transformed from transmittance to absorbance, facilitating a more direct interpretation of molecular vibrations and chemical composition, given the logarithmic relationship between transmittance and absorbance which enhances spectral feature visibility (Campanella *et al.*, 2021). To further refine the analysis, Principal component analysis (PCA) and loading plots were generated using Statistics and Machine Learning Toolbox (MathWorks, Natick, MA, USA) in MATLAB. Prior to PCA, spectra were pre-processed using standard normal variate (SNV) correction, Savgol filtering, and mean-centering to reduce noise and baseline variations. PCA enabled the identification of sample clusters and highlighted the dominant spectral features accounting for the greatest variance among samples, thereby improving the interpretability of process-induced differences. The associated loading plots were instrumental in identifying specific wavenumbers responsible for sample differentiation, allowing for the pinpointing of key spectral regions contributing to observed variations, particularly along the first two principal components (PC1 and PC2), which captured the most significant spectral variance within the dataset.

2.4. Quantification assays

2.4.1. dsDNA

Two versions of the DNA quantification protocol were employed (Table 4): (1) version A – followed the manufacturer instructions of the GK03 GRS Genomic DNA Kit (GRISP™). Briefly, lyophilized tissue samples were placed in 1.5 mL microcentrifuge tubes, followed by the addition of 200 µL Buffer BC2 and 60–100 µL of 20 mg/mL proteinase K. Samples were vortexed and incubated at 60°C for at least 30 minutes with intermittent inversion for digestion. Subsequently, 200 µL Buffer TC1 was added, vortexed, and incubated again at 60°C for 20 minutes. After cooling, 4 µL of 10 mg/mL RNase A was introduced, followed by vortexing and a 5-minute RT incubation. Lysates were then mixed with 200 µL absolute EtOH and vortexed before transfer to a gDNA Plus Mini Spin Column in a collection tube, centrifuged at 16,000 g for 2 minutes. Columns were washed sequentially with 400 µL Wash Buffer 1 and 600 µL Wash Buffer 2 (both followed by centrifugation), then dried by centrifugation for 3 minutes. Subsequently, a preheated Elution Buffer was carefully applied to the center of the membrane within the spin column, which had been positioned in a new 1.5 mL microcentrifuge tube. Following a 5-minute incubation at room temperature, a final centrifugation step of 30 seconds was performed to elute the purified genomic DNA into the microcentrifuge tube; and (2) version B – 250 µL of lysis buffer—comprising 10 mM Tris-HCl, 1 mM EDTA, and 0.5% SDC—along with approximately 100 µL of 20 mg/mL proteinase K, were added to the lyophilized tissue in a microcentrifuge tube. The mixture was vortexed thoroughly and incubated at 60°C for a minimum of 30 minutes with periodic inversion to ensure complete digestion. After digestion, 1% SDC and 0.3 M NaCl were added for protein precipitation. The mixture was centrifuged twice at 16,000 g for 10 minutes each to ensure protein removal. Following the addition of 4 µL of 10 mg/mL RNase A, the mixture was vortexed and incubated at RT for 5 minutes. Subsequently, 600 µL of absolute EtOH was added and vortexed vigorously for 10 seconds. The GK03 GRS Genomic DNA Kit was then employed, transferring the mixture to a gDNA Plus Mini Spin Column placed in a collection tube. After centrifugation at approximately 16,000g for 2 minutes, 400 µL of Wash Buffer 1 and 600 µL of Wash Buffer 2 were each applied twice, with a 30-second centrifugation following each wash to ensure thorough removal of contaminants. The column matrix was then centrifuged for an additional 3 minutes to ensure complete dehydration. Finally, a preheated Elution Buffer was added as described in version A to elute the purified genomic DNA.

In addition, the applications of meniscal tissue dry weight and elution buffer volume varied in each decellularization protocol. For DNA quantification, the nanophotometer was first blanked

with the same Elution Buffer. Then, 3 µL of the eluted DNA was loaded onto the measurement platform, which was thoroughly cleaned with DNA-free water between samples to prevent cross-contamination.

Table 4 – Overview of the DNA quantification protocols employed, including corresponding meniscal sample dry weights and elution buffer volumes for each decellularization protocol.

PV	1	2	3	4
Version of the DNA quantification protocol	**A**	**A**	**B**	**A**
Range of sample dry weight (mg)	5 – 7	20 – 25	5 – 7	3 – 5
Volume of elution buffer (µL)	100	40	100	100

2.4.2. GAGs

GAGs quantification was performed using the Blyscan™ sulfated GAG assay kit. Lyophilized meniscal samples, weighing approximately 4 to 6 mg, were placed into microcentrifuge tubes. Subsequently, 1 mL of papain digestion solution—composed of 0.2 M sodium phosphate buffer (pH 6.4), sodium acetate, EDTA, and cysteine HCl—was added to each sample, followed by incubation at 65°C for a minimum of 3 hours to facilitate tissue digestion. After digestion, samples were centrifuged at 13,000g for 10 minutes, and the supernatant was carefully transferred to new tubes. Aliquots of 10 to 100 µL of supernatant were diluted with deionized water to a final volume of 100 µL in separate tubes. Then, 1 mL of Blyscan dye reagent was added to each aliquot, which was mixed by inversion and gentle mechanical agitation for 30 minutes, allowing the formation and precipitation of the sulfated GAG-dye complex. Samples were centrifuged for 10 minutes—extended by an additional 5 minutes if needed—to pellet the insoluble sulfated GAG-dye complex effectively. The supernatant was carefully decanted, and 500 µL of dissociation reagent was added to release the bound dye into solution, facilitated by vortexing. Following complete dissolution, samples were centrifuged for 5 minutes to remove foam. Finally, 200 µL of each sample was transferred to individual wells of a 96-well microplate, and absorbance was measured at 656 nm using a microplate reader.

2.4.3. Soluble collagen

Quantitative analysis of soluble collagen in meniscal samples was conducted using the Sircol™ Soluble Collagen Assay Kit. Lyophilized tissue samples weighing approximately 4 to 6 mg were placed in microcentrifuge tubes, to which 200 µL of acid-pepsin extraction solution was added. Samples were incubated overnight at 4°C with continuous mechanical agitation to facilitate collagen solubilization. Following incubation, samples were centrifuged at 13,000g

for 10 minutes to pellet residual tissue debris. A 100 µL aliquot of the resulting supernatant was transferred to a fresh tube for soluble collagen quantification, while the remaining supernatant and pellet were stored at 4°C for subsequent insoluble collagen analysis.

To each aliquot, 1 mL of Sircol Dye Reagent was added to saturate collagen molecules, followed by gentle mechanical agitation for 30 minutes to allow formation of the collagen-dye complex. Samples were then centrifuged for 10 minutes to pellet the complex, after which the supernatant was carefully discarded. The collagen-dye pellet was washed with 750 µL of diluted ice-cold Acid-Salt Wash Reagent to remove unbound dye, followed by a second 10-minute centrifugation and removal of wash fluid. Subsequently, 1000 µL of Alkali Reagent was added to release the bound dye into solution, assisted by vortex mixing. Finally, 200 µL of each sample was transferred into individual wells of a 96-well microplate, and absorbance was measured at 556 nm using a microplate reader.

2.4.4. Insoluble collagen

Insoluble collagen quantification in meniscal samples was performed using the Sircol™ Insoluble Collagen Assay Kit. Approximately 20 to 30 mg of wet tissue, remaining after the acid-pepsin extraction used for soluble collagen analysis, was weighed and placed into screw-capped, round-bottom 2 mL digestion tubes. To each sample, 50 µL of Fragmentation Reagent per milligram of wet tissue was added. Samples were incubated at 65°C for 2 to 3 hours with periodic inversion to facilitate digestion, followed by centrifugation at 13,000g for 10 minutes. Thereafter, 100 µL of supernatant was transferred to fresh microcentrifuge tubes, and 1 mL of Sircol Dye Reagent was added. The mixtures were vortexed and subjected to gentle mechanical agitation for 30 minutes to allow formation of the collagen-dye complex. Samples were centrifuged for 10 minutes, after which the supernatant was carefully decanted. Subsequently, 750 µL of ice-cold Acid-Salt Wash Reagent was added to each pellet to remove unbound dye, followed by a 10-minute centrifugation and removal of the wash solution. Finally, 1 mL of Alkali Reagent was added to dissolve the collagen-bound dye, assisted by vortex mixing. After complete dissolution, 200 µL of each sample was transferred into individual wells of a 96-well microplate, and absorbance was measured at 556 nm using a microplate reader.

2.5. Statistical analysis

Numerical results are presented as mean ± SD. Statistical analyses were conducted using GraphPad Prism 8.0 (GraphPad Software, La Jolla, CA). Data normality was assessed by the Shapiro-Wilk test. For DNA quantification in PV4, two separate Mann–Whitney U tests were performed to compare the $scCO_2$-treated sample with its control and the detergent-treated

sample with its respective control. For all other biological quantification assays, differences among groups were evaluated using the Kruskal–Wallis test followed by Dunn's multiple comparisons test. Statistical significance was indicated as *$p < 0.05$, **$p < 0.01$, and ***$p < 0.001$.

3. Results

A comparative analysis was conducted across the developed protocols. The evaluation of decellularization efficiency was based on the quantification of residual dsDNA within the tissue matrices. In addition, the preservation of ECM components, critical for maintaining the mechanical and biological functionality of the scaffold, was assessed both quantitatively and qualitatively through the quantification of collagen and GAG content and FTIR spectroscopy, respectively.

Following decellularization, the meniscal tissues exhibited an evident whitening (Figure 7B) compared to the native control (Figure 7A), while the overall conformation and structural integrity were preserved.

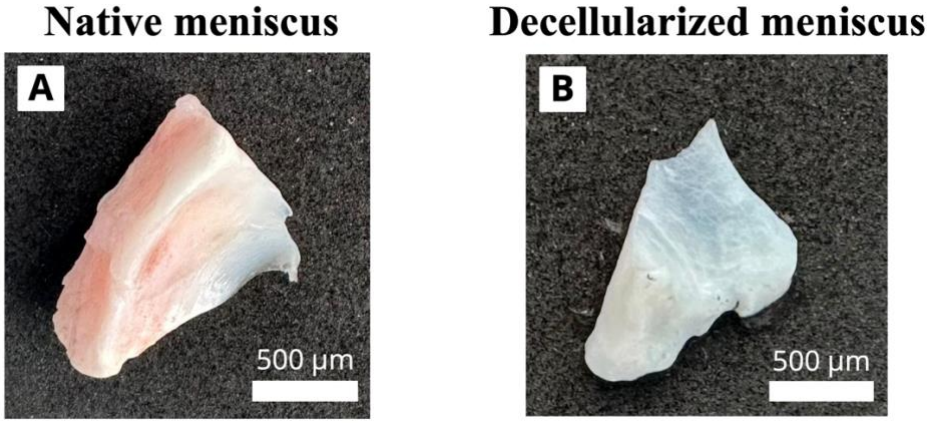

Figure 7 – Representative macroscopic images of the (A) native porcine meniscus and (B) decellularized porcine meniscus in all developed decellularization protocols.

3.1. Protocol version 1 (PV1)

In PV1 (Figure 8), samples underwent two different washing modes—static and continuous—and were subjected to 1 cycle (PV1_Static-1 and PV1_Continuous-1) or 2 cycles (PV1_Static-2 and PV1_Continuous-2) of $scCO_2$ treatment. Among these, the PV1_Static-2 sample exhibited the lowest residual dsDNA content at 583.87 ± 53.74 ng/mg, while the PV1_Continuous-2 sample had the highest at 765.15 ± 170.00 ng/mg. The PV1_Static-1 and PV1_Continuous-1 samples presented intermediate values, with 735.61 ± 199.94 ng/mg and 719 ± 83.96 ng/mg of residual dsDNA, respectively. Despite these subtle variations, no statistically significant differences were observed across the four sample groups, inferring an ineffective decellularization efficiency in PV1 and no differences comparing a static setup with a continuous setup.

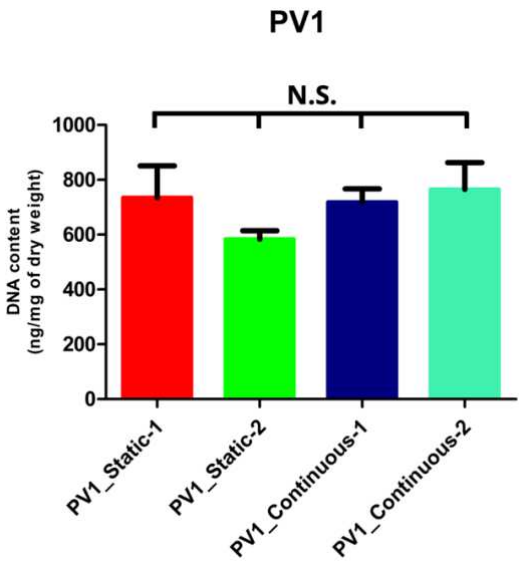

Figure 8 – DNA quantification of samples subjected to PV1.

Regarding FTIR analysis (Figure 9), initial examination of the spectra revealed generally similar overall patterns and intensities across samples, particularly within the two most relevant spectral regions: approximately 800–1700 cm^{-1} and 2800–3600 cm^{-1}. The lack of substantial spectral variation suggests that the functional biomolecules within the ECM may have been largely preserved following treatment. Nonetheless, subtle differences were detected. Specifically, two prominent peaks were observed in the spectrum of the PV1_Static-1 sample at 2918 cm^{-1} (corresponding to the amide B band of collagen) and 2850 cm^{-1} (corresponding to the amide B band of collagen and the asymmetric stretching vibrations of CH_2 and CH_3 groups) (as detailed in Appendix F). Furthermore, the PV1_Static-2 sample exhibited a distinct peak at 1046 cm^{-1}, attributed to the structural backbone and glycosidic linkages of GAGs (as detailed in Appendix F). This suggests that the static mode washing yielded samples with moderately cleaner matrices (Li *et al.*, 2024).

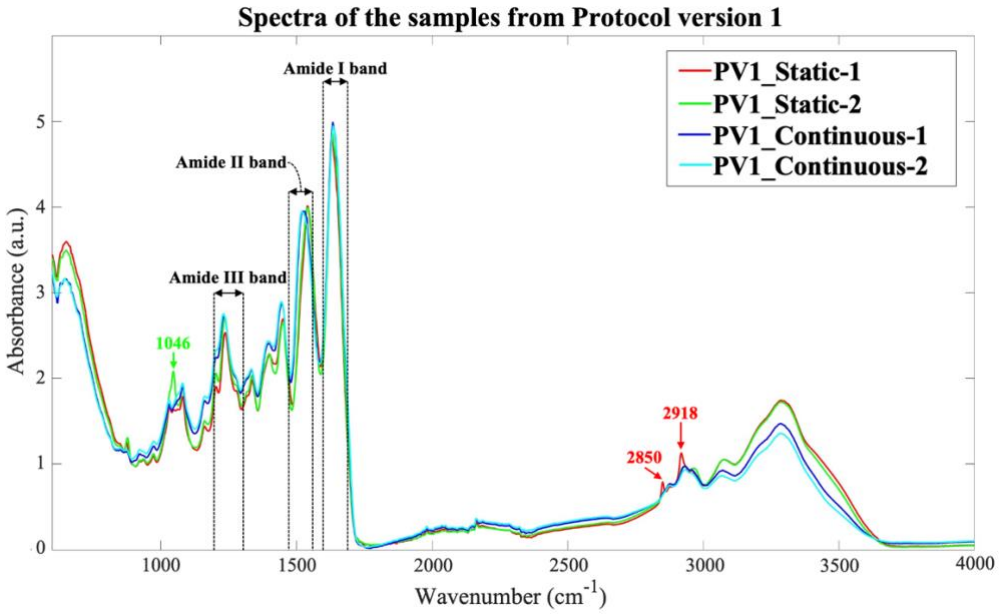

Figure 9 – Spectral profiles of the samples from PV1, indicating key vibrational bands and unique wavenumbers.

Analysis of the PCA results for PV1 (Figure 10) revealed that the primary differences in spectral profiles are distinguished along PC1, which accounts for 83.71% of the total variance. This component effectively separates the Static-mode washing samples (PV1_Static-1 and PV1_Static-2) from the Continuous-mode washing samples (PV1_Continuous-1 and PV1_Continuous-2). PC2, explaining a smaller proportion of variance (15.72%), primarily differentiates between the PV1_Static-1 and PV1_Static-2 samples, whereas the samples where the continuous washing steps (PV1_Continuous-1 and PV1_Continuous-2) were applied cluster closely near the origin along this component. These clustering patterns correspond well with the spectral data shown in Figure 8, where the PV1_Static-1 and PV1_Static-2 samples exhibit similar peak profiles and intensities, while the PV1_Continuous-1 and PV1_Continuous-2 samples display highly consistent spectral patterns.

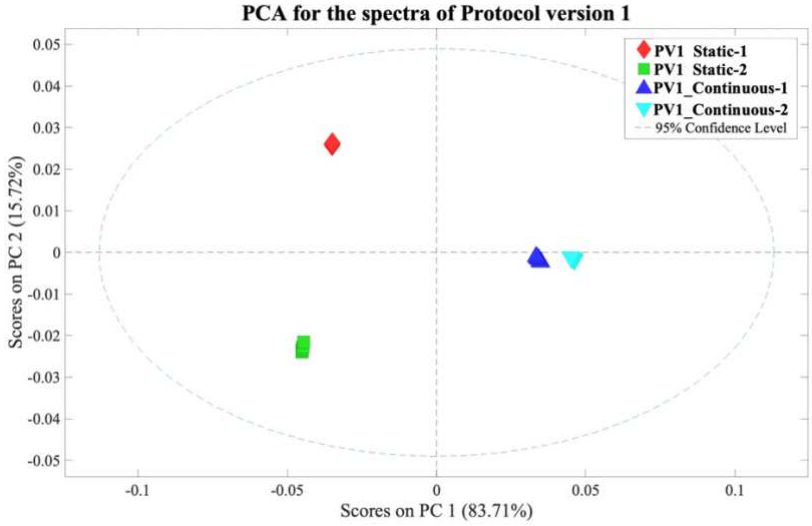

Figure 10 – PCA score plot of the FTIR spectra obtained from samples treated under PV1.

To further elucidate the key contributors to the variance between the two washing modes—static and continuous—the PCA loading plot based on PC1 (Figure 11), alongside band assignments summarized in Table 5, was analyzed to correlate spectral features with the biochemical and structural properties of the samples. Notably, regarding genetic material, the asymmetric PO_2^- stretching of the phosphate backbone appears on both sides of PC1, with the peak at 1238 cm^{-1} in the positive PC1 and the peak at 1220 cm^{-1} in the negative PC1. Similarly, the symmetric PO_2^- stretching of the phosphate backbone and the C–OH group vibrations in the pentose sugar are observed on both sides of PC1, indicated by the peaks at 1044 cm^{-1} (positive PC1) and 1062 cm^{-1} (negative PC1). Although it is not definitively clear which sample group exhibits greater prominence of these features, these spectral differences suggest structural alteration of genetic material. Asymmetric phosphate and C–OH group vibrations serve as established markers of the transition in DNA secondary structure from B-form—the most common and stable conformation under physiological conditions—to A-form, which exhibits tighter chromatin packaging due to its interaction with nuclear proteins and ECM (Paston *et al.*, 2020; Mustafa *et al.*, 2022; Bonnet *et al.*, 2010). When coupled with symmetric phosphate stretching, these changes indicate tighter nucleic acid packaging (Sumi *et al.*, 2021; Quinn *et al.*, 2022).

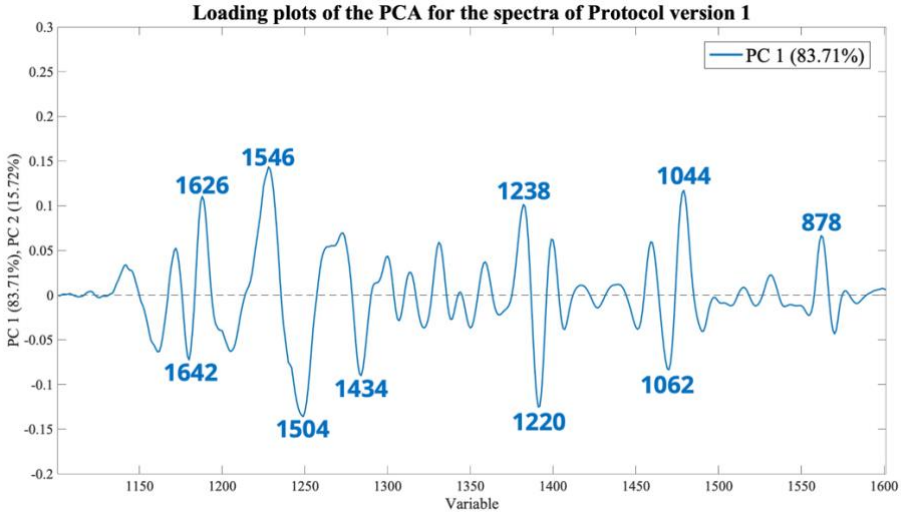

Figure 11 – Loading plot of PC1 obtained from PCA for the spectra of PV1, highlighting the key wavenumbers contributing to the principal component separation.

Table 5 – Peak band assignments corresponding to the major spectral features contributing to PC1 in the PCA of PV1.

Side of PC1	Peak position (cm^{-1})	Functional group vibrations	Corresponding biomolecules
Positive	1626	Amide I band	Collagen
	1546	Amide II band	Collagen
		Uronic acid	GAGs
	1238	Amide III band	Collagen
		SO_3^- sulfated GAGs	GAGs
		P=O asymmetric stretching	Lipid
		Phosphate backbone	Genetic materials
	1044	Structural backbone and glycosidic linkage	GAGs
		Phosphate backbone	Genetic materials
		Pentose sugar	
	878	Pentose sugar	Genetic materials
Negative	1642	Amide I band	Collagen & Elastin
	1504	Amide II band	Collagen
	1434	Uronic acid	GAGs
	1220	Amide III band	Collagen
		SO_3^- sulfated GAGs	GAGs
		Phosphate backbone	Genetic materials
	1062	Structural backbone and glycosidic linkages	GAGs
		Phosphate backbone	Genetic materials
		Pentose sugar	

3.2. Protocol version 2 (PV2)

For PV2 (Figure 12), which included up to nine cycles of $scCO_2$ treatment, the dsDNA quantification was performed after the 1st cycle (PV2_1), 2nd cycle (PV2_2), 5th cycle (PV2_5), 8th cycle (PV2_8) and 9th cycle (PV2_9). The results revealed that a gradual reduction in DNA content was observed with increasing cycles. The Control sample contained 147.04 ± 37.52 ng/mg of dsDNA, while the PV2_1, PV2_2, PV2_5, PV2_8 and PV2_9 samples exhibited

values of 111.60 ± 12.88 ng/mg, 95.84 ± 26.25 ng/mg, 79.26 ± 21.42 ng/mg, 67.72 ± 10.44 ng/mg, and 52.65 ± 10.85 ng/mg, respectively. Notably, the PV2_9 sample demonstrated a statistically significant decrease in DNA content compared to the control sample, suggesting an effective decellularization after the performance of 9 cycles of $scCO_2$ treatment.

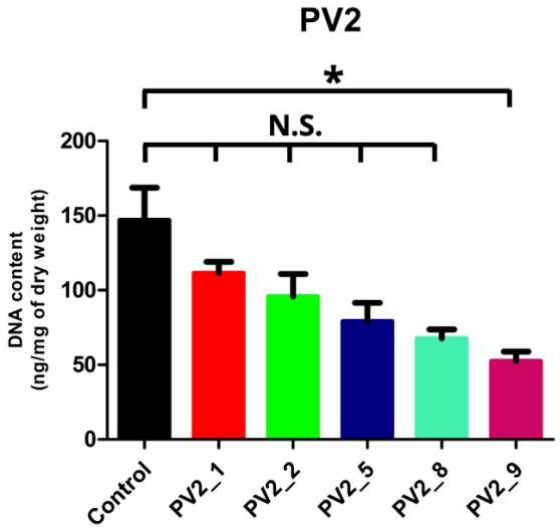

Figure 12 – DNA quantification of samples subjected to PV2.

Regarding the FTIR spectra from PV2 (Figure 13), analysis of key ECM biomolecules—particularly collagen—revealed that the characteristic amide bands displayed relatively consistent patterns and intensities across all samples. However, moderate variations in peak intensities and slight spectral shifts were observed, most notably in the spectrum of the 8h $scCO_2$-treated sample (PV2_8). For instance, the Amide B and Amide I bands appeared slightly more intense in this sample compared to the others. Beyond collagen, the PV2_8 sample also exhibited distinct variations in molecular vibrations associated with GAGs. Notably, the peaks at 1082 cm^{-1} and 1046 cm^{-1}—corresponding to the structural backbone and glycosidic linkages of GAGs—exhibited markedly increased intensity compared to the control. Furthermore, the peak at 878 cm^{-1} was also enhanced. While this region partially reflects pentose sugar ring vibrations from nucleic acids, it is predominantly associated with proteoglycans and aggrecan groups characteristic of articular cartilage (Vidal *et al.*, 2016). These enhanced peak intensities and sharper spectral definition may reflect the reduction of background signals from residual impurities, thereby resulting in a cleaner matrix particularly in the PV2_8 sample (Li *et al.*, 2024).

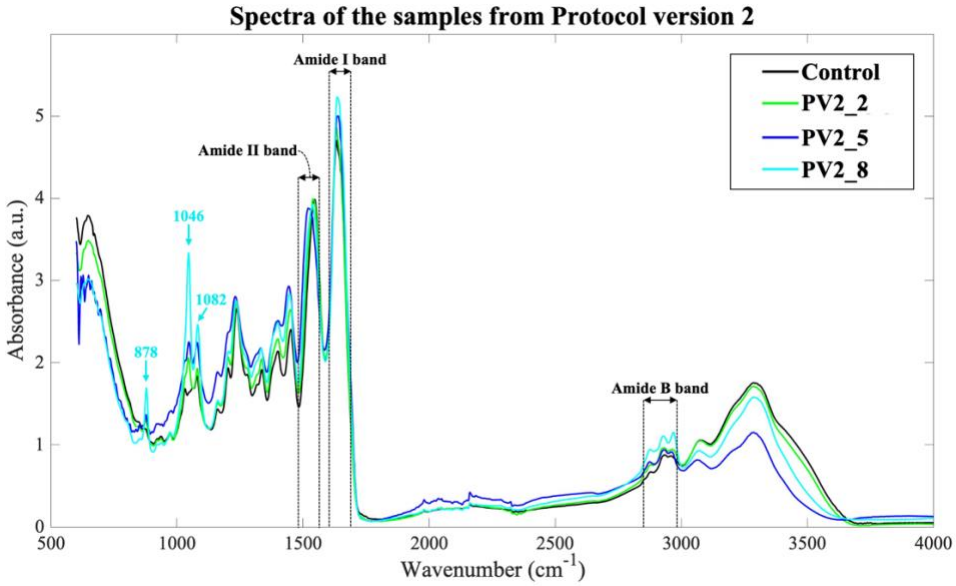

Figure 13 – Spectral profiles of the samples from PV2, annotating unique vibrational bands and wavenumbers.

3.3. Protocol version 3 (PV3)

Subsequently, a detergent treatment (PV3+Detergent) was applied in PV3 (Figure 14). Both treated samples demonstrated lower remaining DNA content compared to the control sample, which exhibited 222.24 ± 66.44 ng/mg. Notably, the PV3 sample (90.74 ± 4.92 ng/mg) showed a moderately lower DNA content than the sample with an additional detergent treatment (PV3+Detergent), whose residual dsDNA was assessed to be 110.19 ± 34.45 ng/mg. However, no statically significant differences were discovered.

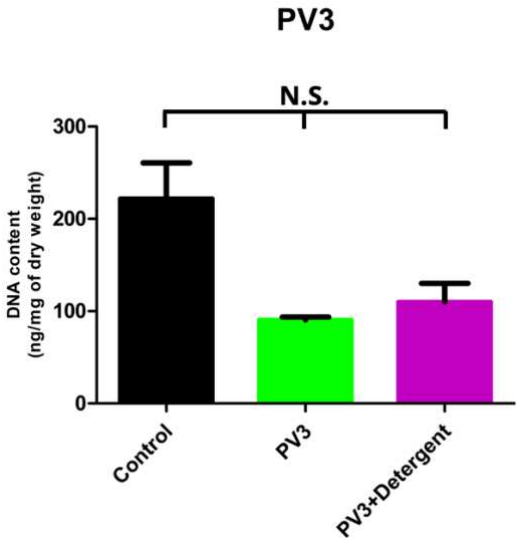

Figure 14 – DNA quantification of samples subjected to PV3.

In the FTIR spectra from PV3 (Figure 15), both treated samples (PV3 and PV3+Detergent) exhibited overall spectral patterns and tendencies comparable to those of the control sample. However, within the spectral region spanning 1200 cm^{-1} to 1700 cm^{-1}, which includes characteristic vibrations of key functional groups such as the Amide I, Amide II, and Amide III bands (primarily associated with collagen and elastin), as well as uronic acid vibrations indicative of GAGs (as detailed in Appendix F), the treated samples displayed relatively enhanced intensity compared to the control, suggesting the production of cleaner matrices after the treatments in PV3.

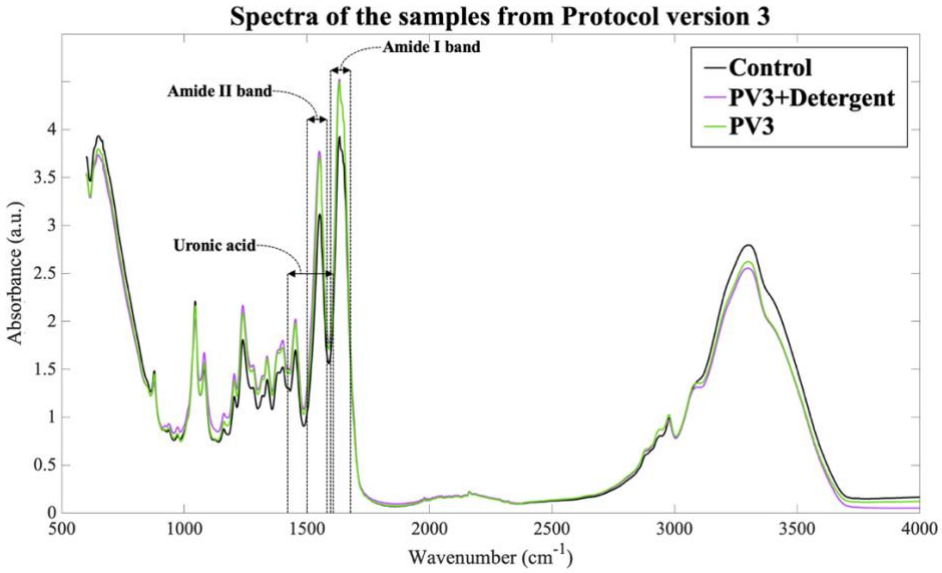

Figure 15 – Spectral profiles of the samples from PV3, with annotations indicating key vibrational bands.

Regarding the PCA results from PV3 (Figure 16), PC1 accounted for 94.61% of the total variance and primarily distinguished the control sample from the PV3+Detergent sample, with the PV3 sample positioned near the zero line of PC1. It reveals that the PV3 sample with an additional detergent treatment (PV3+Detergent) exhibited the most spectral variance compared to the control sample. Notably, since the detergent treatment was applied along with the $scCO_2$ cyclic treatment, the spatial arrangement of the three samples in the PCA plot visually reflects the progression from native tissue (Control sample) through $scCO_2$ treatment (PV3 sample) to the detergent-treated sample (PV3+Detergent sample).

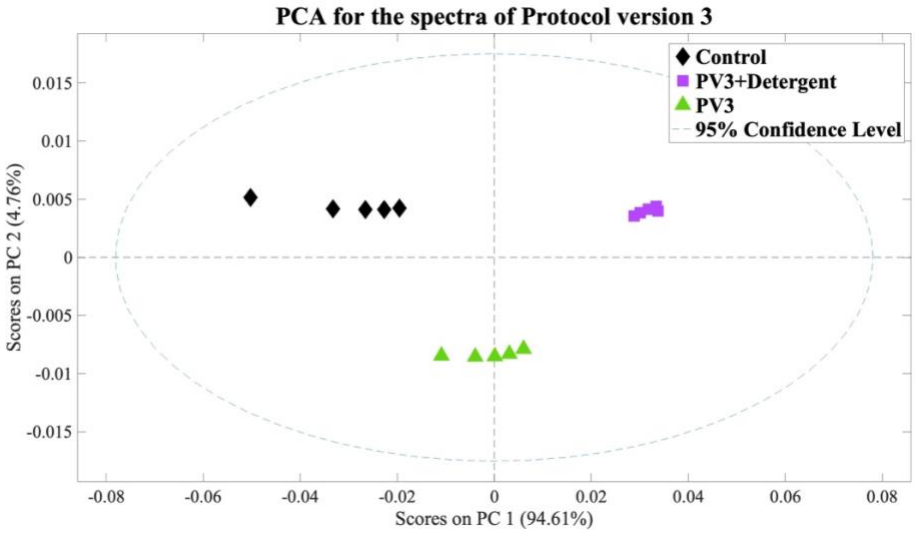

Figure 16 – PCA score plot of the FTIR spectra obtained from samples treated under PV3.

To further investigate the biomolecular contributors to the differentiation along PC1, whose spectra showed markedly elevated variance, the corresponding PCA loading plot was examined (Figure 17), followed by the establishment of the band assignments (Table 6), as highlighted from the Appendix F. On the negative side of PC1, which correlates with the control sample, the presence of collagen is indicated by the Amide I and Amide II band vibrations, while elastin and GAGs are presented by the Amide II band and uronic acid following structural backbone vibrations, respectively. In contrast, the positive side of PC1, corresponding to the PV3+Detergent sample, did not exhibit any molecular features associated with collagen and revealed only a single feature related to GAGs. This suggests that the captures of these two pivotal ECM components in porcine meniscus are not predominant in the detergent-treated matrix, potentially reflecting conformational alterations induced by the treatment process.

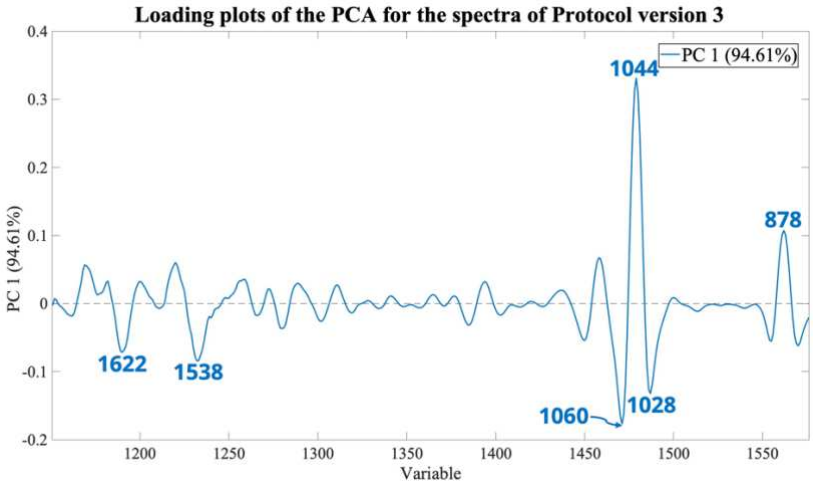

Figure 17 – Loading plot of PC1 obtained from PCA for the spectra of PV3, highlighting the key wavenumbers contributing to the principal component separation.

Table 6 – Peak band assignments corresponding to the major spectral features contributing to PC1 in the PCA of PV3.

Side of PC1	Peak position (cm^{-1})	Functional group vibrations	Corresponding biomolecules
Positive	1044	Structural backbone and glycosidic linkages	GAGs
		Phosphate backbone and pentose sugar	Genetic materials
	878	Pentose sugar	Genetic materials
Negative	1622	Amide I band	Collagen
	1538	Amide II band	Collagen
			Elastin
		Uronic acid	GAGs
	1060	Structural backbone and glycosidic linkages	GAGs
		Phosphate backbone and pentose sugar	Genetic materials
	1028	Structural backbone and glycosidic linkages	GAGs
		Pentose sugar	Genetic materials

3.4. Protocol version 4 (PV4)

3.4.1. Pre-sterilization assessment

Ultimately, for PV4 (Figure 18), two different sample architectures, namely cubic (PV4_CUBE) and sliced shape (PV4_SLICE), were tested. In addition, PV4 was performed in another batch with the addition of ethanol (PV4_CUBE-Ethanol and PV4_SLICE-Ehtanol) as co-solvent during the $scCO_2$ treatment.

For the batch with only $scCO_2$ in the reactor, the PV4_CUBE sample exhibited a statistically significant reduction in DNA content, with 88.74 ± 10.25 ng/mg, compared to the control sample, which contained 315.00 ± 5.34 ng/mg. The PV4_SLICE sample retained 105.82 ± 13.59 ng/mg of DNA within the matrix, which did not demonstrate significant decrease of DNA content from the control sample.

Furthermore, while ethanol was applied as a co-solvent, the PV4_CUBE-Ethanol sample exhibited a residual dsDNA content of 174.41 ± 42.02 ng/mg, while PV4_SLICE-Ethanol demonstrated 159.36 ± 30.40 ng/mg. The corresponding control sample contained 518.44 ± 183.25 ng/mg of dsDNA. Although both treated samples revealed a reduction of DNA content after the decellularization process, no significant differences were observed when comparing to the control sample, suggesting that the inclusion of ethanol did not appear to enhance decellularization efficiency.

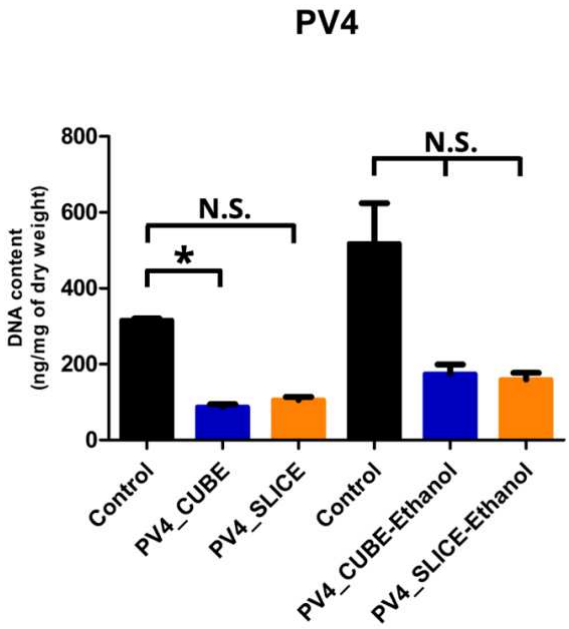

Figure 18 – DNA quantification of samples subjected to PV4.

Given that PV4 was elected as optimized protocol at this stage based on the dsDNA quantification results, the quantitative assessment of ECM preservation was performed. In porcine menisci, aside from their elevated water content, the tissue composition includes approximately 2.5% GAGs and 30% collagen (Gonzalez-Leon *et al.*, 2022). Therefore, assessing the retention of these key ECM components following decellularization is of critical importance. The GAGs, soluble collagen, and insoluble collagen content were assessed in the presence and absence of ethanol as co-solvent (Figure 19).

Regarding GAGs content (Figure 19A), the PV4_CUBE sample preserved 14.05 ± 3.85 µg/mg, while the PV4_SLICE sample retained 13.99 ± 0.81 µg/mg. When co-solvent was employed, the PV4_CUBE-Ethanol and PV4_SLICE-Ethanol retaining 5.87 ± 2.54 µg/mg and 9.27 ± 2.94 µg/mg of GAGs, respectively. In this context, the addition of ethanol appeared to slightly reduce GAGs content preservation; however, no statistically significant differences were observed compared to their respective native tissues.

Regarding soluble collagen (Figure 19B) and insoluble collagen (Figure 19C), the retention trend was preserved. Accordingly, the inclusion of ethanol, as well as the shape of the samples, did not affect the preservation of these key biomolecular components since no statistically significant differences were observed comparing with their respective control samples. Briefly, the soluble collagen content appeared to decrease more in the PV4_SLICE sample, namely from 5.86 ± 0.89 ug/mg to 1.74 ± 0.84 ug/mg, while the PV4_CUBE sample preserved

considerably 5.40 ± 1.53 ug/mg. With the addition of ethanol, the PV4_CUBE-Ethanol sample preserved slightly more soluble collagen content, namely of 3.49 ± 1.04 ug/mg compared to the control sample (3.55 ± 2.26 ug/mg), while the PV4_SLICE-Ethanol samples decreased to 3.07 ± 0.76 ug/mg. Concerning insoluble collagen, the PV4_CUBE sample presented moderate decrease to 163.80 ± 69.65 µg/mg from 285.66 ± 45.56 µg/mg, while the PV4_SLICE sample preserved 214.62 ± 53.85 µg/mg. PV4_CUBE-Ethanol and PV4_SLICE-Ethanol samples preserved equitable insoluble collagen content, corresponding to 211.36 ± 30.22 µg/mg and 210.05 ± 28.12 µg/mg, respectively. Nonetheless, both groups demonstrated a modest reduction compared to the control sample (268.58 ± 119.63 µg/mg).

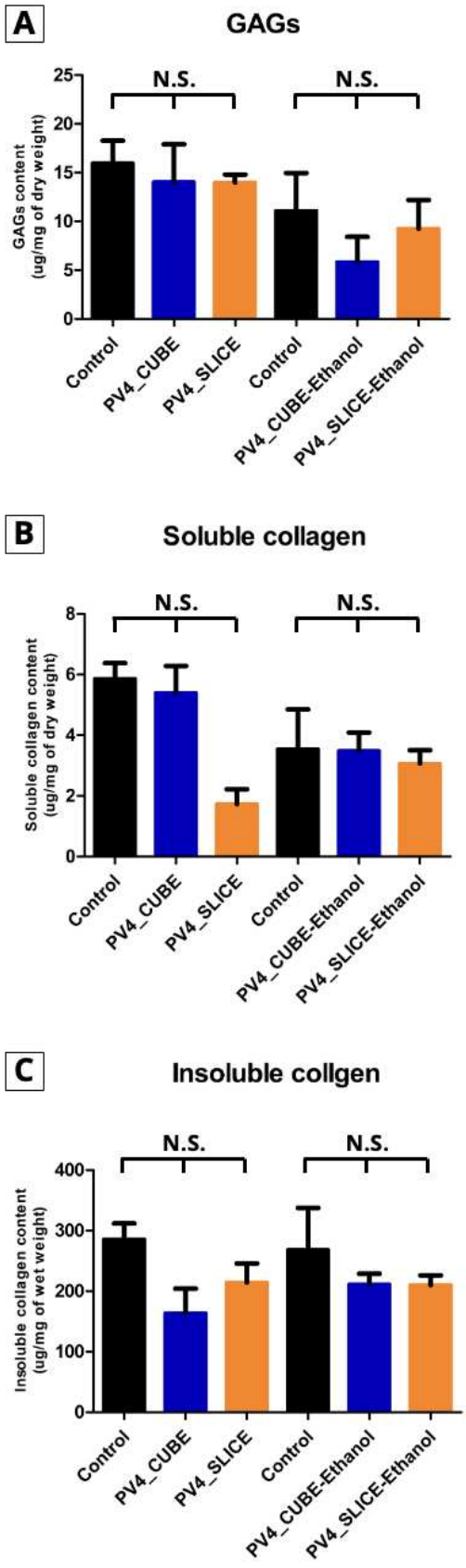

Figure 19 – Quantification of (A) GAGs, (B) soluble collagen and (C) insoluble collagen content in PV4.

To minimize overestimation of spectral variance generated by biological sample variability, FTIR analyses and the corresponding chemometric evaluations for ethanol-free and ethanol treated samples were performed independently.

Analysis of the FTIR spectra from PV4 (Figures 20 and Figure 22) reveals that the region spanning approximately 900 to 1150 cm^{-1}—typically associated with carbohydrate vibrations, including glycosidic linkages and sulfated sugar moieties present in GAGs (Brézillon *et al.*, 2014)—exhibited distinct patterns and tendencies compared to the corresponding spectral regions observed in earlier protocols, suggesting the variations of biomolecular arrangement and conformation of GAGs in the samples between PV4 and the previous decellularization protocols.

In PV4 without the application of ethanol (Figure 20), the FTIR spectra demonstrated that the PV4_CUBE sample exhibited the highest intensity in the Amide I and Amide II bands, which correspond to molecular vibrations of collagen. Conversely, the PV4_SLICE sample displayed a relatively stronger peak at 1450 cm^{-1}, attributed to the bending vibration of CH_2 groups in collagen (Wang *et al.*, 2018). Despite these variations in peak intensities among the different samples, the overall spectral patterns and trends remained largely unchanged.

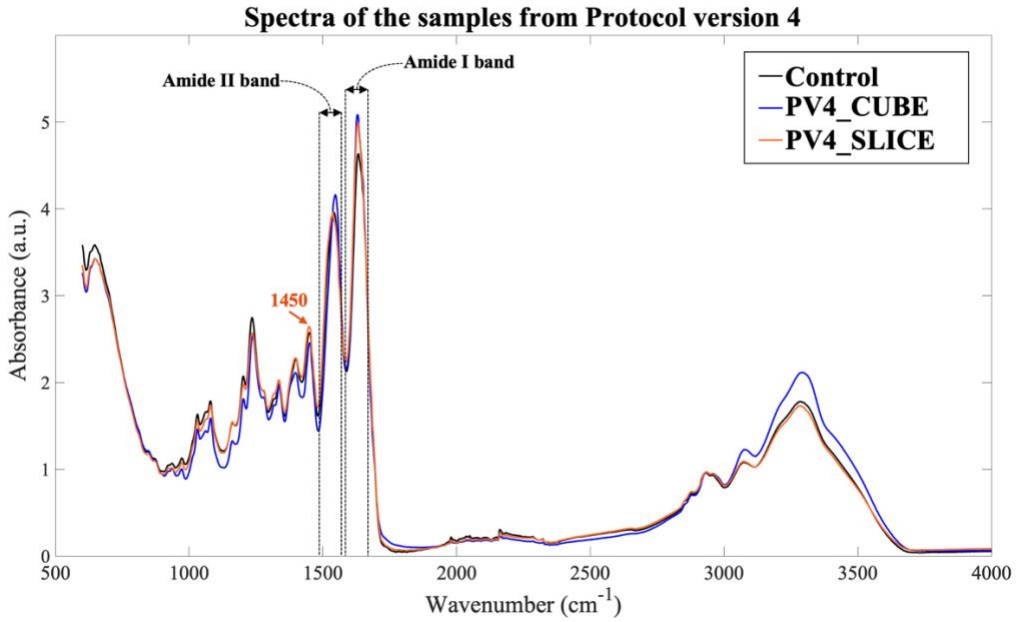

Figure 20 – Spectral profiles of the samples from PV4 WITHOUT ethanol as co-solvent, annotating unique vibrational bands and wavenumbers.

Regarding the PCA resulting from the spectra of PV4 without the ethanol as co-solvent (Figure 21A), PC1 accounts for 76.92% of the total spectral variance and primarily differentiates

between the PV4_CUBE and PV4_SLICE samples, while the control sample is positioned close to the PC1 zero axis. This suggests that the majority of spectral variance induced by the decellularization procedure was attributed to biochemical differences between the two sample geometries (PV4_CUBE and PV4_SLICE), rather than between these two treated samples and native tissue. According to the loading plot (Figure 21B) and corresponding molecular vibration assignments (Table 7), GAG-associated vibrations are more prominently represented on the negative side of PC1, corresponding to the PV4_CUBE sample. Furthermore, while the presence of Amide III band vibrations—related to collagen—were exclusively significant in the PV4_CUBE sample, Amide I and II bands appeared on both sides of PC1, suggesting no clear dominance in either group.

Concerning PC2, which explains 23.00% of the total variance, it differentiates the control sample (negative side) from both treated samples (positive side), particularly the PV4_SLICE sample. Notably, molecular vibrations associated with collagen and GAGs contributed significantly to this separation (Table 8), with particular emphasis on GAG-related peaks—including those from uronic acid and sulfated groups—being more pronounced in the PV4_CUBE and PV5_SLICE samples. This observation implies the generation of cleaner matrices of these two treated samples due to effective removal of cellular components and other interfering molecules from impurities during decellularization, thereby reducing spectral complexity and enhancing the visibility of low-abundance components such as GAGs in FTIR analysis.

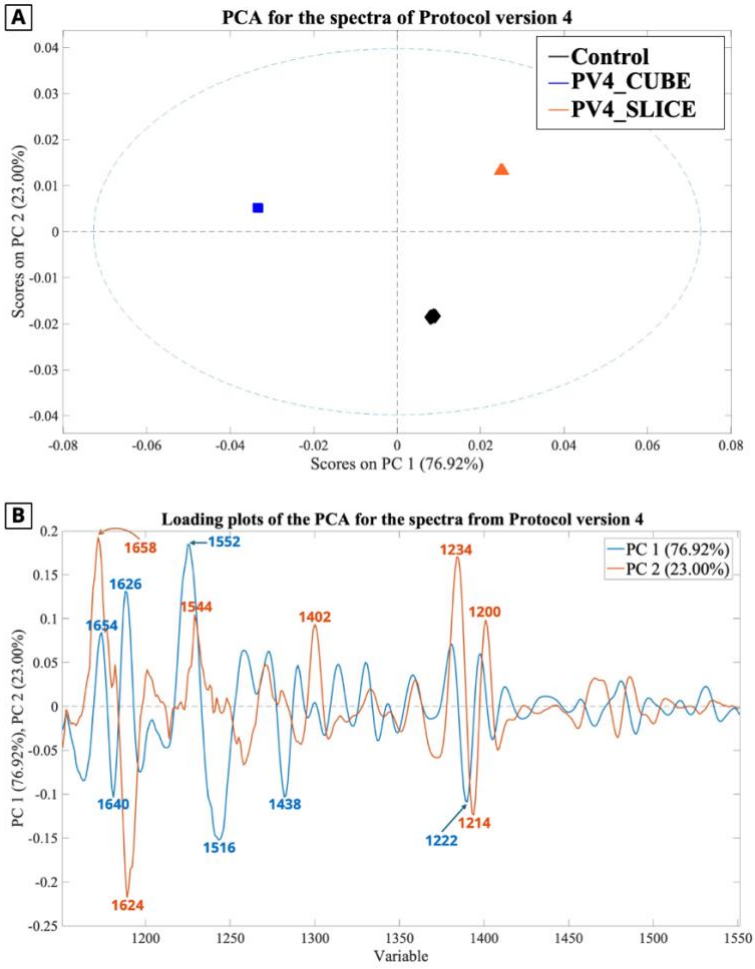

Figure 21 – (A) PCA score plot of the FTIR spectra obtained from samples treated under PV4 WITHOUT ethanol as co-solvent, and its (B) corresponding loading plot, highlighting the key wavenumbers contributing to the principal component separation.

Table 7 – Peak band assignments corresponding to the major spectral features contributing to PC1 in the PCA for PV4 WITHOUT ethanol as co-solvent.

Side of PC1	Peak position (cm^{-1})	Functional group vibrations	Corresponding biomolecules
Positive	1654	Amide I band	Collagen & Elastin
	1626		
	1552	Amide II band	Collagen
		Uronic acid	GAGs
Negative	1640	Amide I band	Collagen & Elastin
	1516	Amide II band	Collagen
		Uronic acid	GAGs
	1438	Uronic acid	GAGs
	1222	Amide III band	Collagen
		SO_3^- sulfated GAGs	GAGs
		Phosphate backbone	Genetic materials

Table 8 – Peak band assignments corresponding to the major spectral features contributing to PC2 in the PCA for PV4 WITHOUT ethanol as co-solvent.

Side of PC2	Peak position (cm^{-1})	Functional group vibrations	Corresponding biomolecules
Positive	1658	Amide I band	Collagen
	1544	Amide II band	Collagen
		Uronic acid	GAGs
	1402	CH_2 bending	Collagen
	1234	Amide III band	Collagen
		SO_3^- sulfated GAGs	GAGs
		Phosphate backbone	Genetic materials
	1200	Amide III band	Collagen
		Phosphate backbone	Genetic materials
Negative	1624	Amide I band	Collagen
	1214	Amide III band	Collagen

When employing ethanol as co-solvent in PV4 (Figure 22), FTIR spectra revealed that the PV4_CUBE-Ethanol sample showed increased intensity in vibrational bands strongly associated with collagen conformation, particularly the Amide I band. In contrast, the PV4_SLICE-Ethanol sample displayed a slight reduction in intensity. Additionally, the peak at 1450 cm^{-1}, attributed to the bending vibration of CH_2 groups in collagen, appeared more intense in both treated samples compared to the control, suggesting structural or compositional alterations in the collagen network.

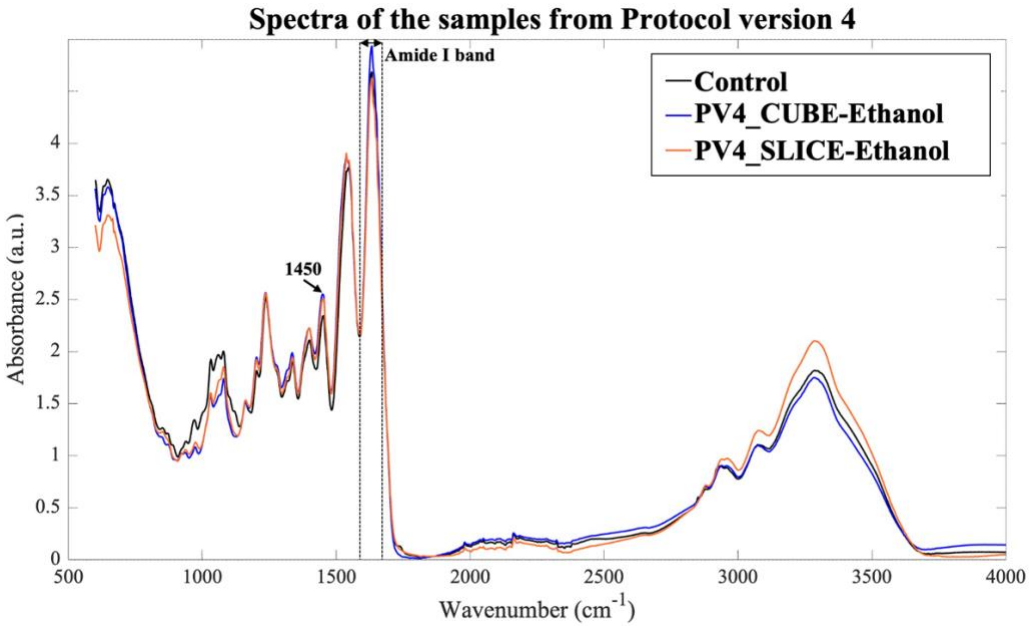

Figure 22 – Spectral profiles of the samples from PV4 WITH ethanol as co-solvent, annotating unique vibrational bands and wavenumbers.

Concerning the PCA results from PV4 with ethanol (Figure 23A), PC1, which accounts for 84.04% of the total variance, primarily distinguishes the control sample from the two treated samples. PC2, contributing 15.77% of the total variance, differentiates between the PV4_CUBE-Ethanol and PV4_SLICE-Ethanol samples, as the control sample is positioned near the zero line of PC2.

To further interpret these variations, the corresponding loading plot was generated (Figure 23B), with band assignments indicating the functional group vibrations of key biomolecules. In the comparison along PC1 (Table 9), both the positive and negative sides revealed similar biomolecular contributions, suggesting no definitive dominance of these components in either group. However, notable differences were observed in the specific vibrational signatures. For instance, in the case of collagen, the PV4_CUBE-Ethanol and PV4_SLICE-Ethanol samples (positive side of PC1) were primarily characterized by Amide I and II bands, whereas the control sample (negative side of PC1) exhibited stronger contributions from Amide II and III bands. Notably, amide I band is crucial for assessing secondary structure of collagen to provide insights into the stability and folding dynamics, while amide III is particularly sensitive to the triple-helical conformation of collagen (Belbachir *et al.*, 2009; Bryan *et al.*, 2007). Regarding PC2 (Table 10), the presence of GAGs appears to be more pronounced in the PV4_CUBE-Ethanol sample (positive side of PC2), while collagen-related features are relatively more dominant in the PV4_SLICE-Ethanol sample (negative side of PC2).

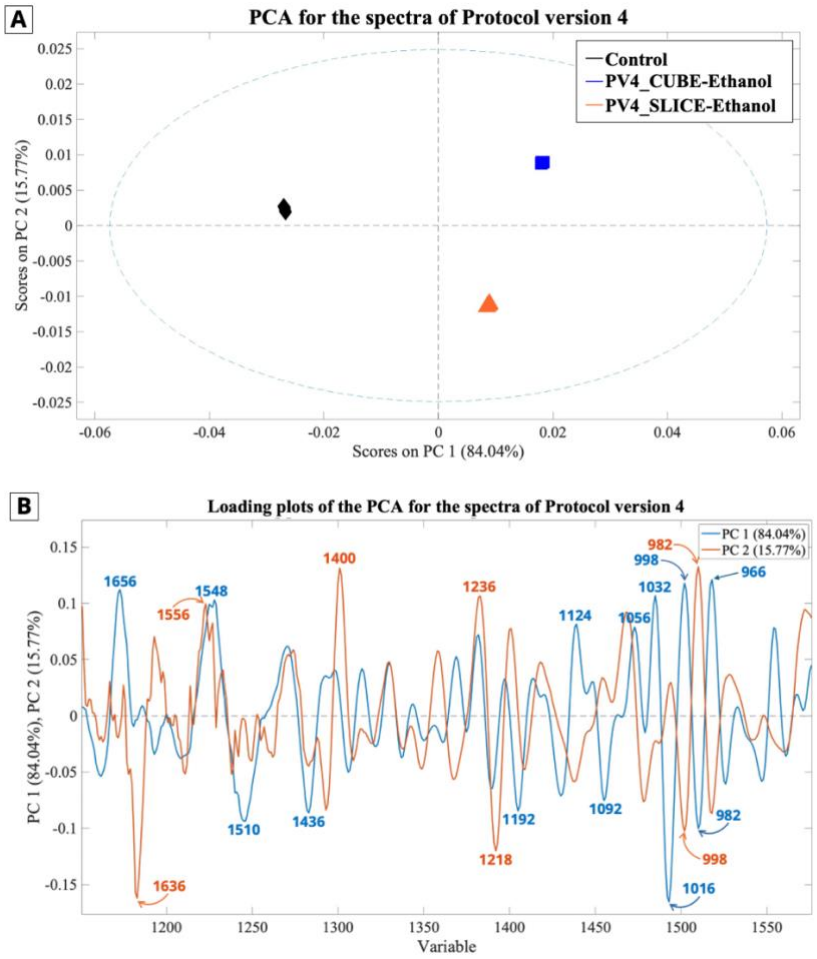

Figure 23 – (A) PCA score plot of the FTIR spectra obtained from samples treated under PV4 WITH ethanol as co-solvent, and its (B) corresponding loading plot, highlighting the key wavenumbers contributing to the principal component separation.

Table 9 – Peak band assignments corresponding to the major spectral features contributing to PC1 in the PCA of PV4 WITH ethanol as co-solvent.

Side of PC1	Peak position (cm^{-1})	Functional group vibrations	Corresponding biomolecules
Positive	1656	Amide I band	Collagen & Elastin
	1548	Amide II band	Collagen
		Uronic acid	GAGs
	1124	Ester linkage of the sulfated group	GAGs
	1056	Structural backbone and glycosidic linkage	GAGs
		Phosphate backbone	Genetic materials
		Pentose sugar	
	1032	Structural backbone and glycosidic linkage	GAGs
		Pentose sugar	Genetic materials
	998	Carboxyl or amine-linked sulfated group	GAGs
	966	Hydrophobic domains	Elastin
		Phosphate backbone	Genetic materials
		Pentose sugar	
Negative	1510	Amide II band	Collagen
		Uronic acid	GAGs
	1436	Uronic acid	GAGs
	1192	Amide III band	Collagen
	1092	Structural backbone and glycosidic linkage	GAGs
		Phosphate backbone	Genetic materials
		Pentose sugar	
	1016	Structural backbone and glycosidic linkage	GAGs
		Pentose sugar	Genetic materials
	982	Carboxyl or amine-linked sulfated group	GAGs

Table 10 – Peak band assignments corresponding to the major spectral features contributing to PC2 in the PCA of PV4 WITH ethanol as co-solvent.

Side of PC2	Peak position (cm^{-1})	Functional group vibrations	Corresponding biomolecules
Positive	1556	Uronic acid	GAGs
	1400	Uronic acid	GAGs
	1236	Amide III band	Collagen & Elastin
		SO_3^- sulfated GAGs	GAGs
		Phosphate backbone	Genetic materials
	982	Carboxyl or amine-linked sulfated group	GAGs
Negative	1636	Amide I band	Collagen
	1218	Amide III band	Collagen
		Phosphate backbone	Genetic materials
	998	Carboxyl or amine-linked sulfated group	GAGs

3.4.2. Post-sterilization assessment

Considering that greater decellularization efficiency and ECM preservation were exhibited without the addition of ethanol as co-solvent, the PV4 samples with only $scCO_2$ in the reactor were conducted with sterilization. The evaluation of ECM preservation after performing sterilization was also assessed through GAGs, soluble collagen, and insoluble collagen quantification (Figure 24).

Following sterilization, the PV4_CUBE-Sterilized sample exhibited 14.24 ± 1.56 ug/mg of GAGs content, while the PV4_SLICE-Sterilized sample demonstrated slight decrease to 12.68 ± 2.06 ug/mg (Figure 23A). When comparing to their respective samples before sterilization, it suggests that sterilization did not significantly affect the preservation of GAGs content in neither cubic- nor sliced-shaped meniscal matrix as no statistic differences were observed.

Regarding the preservation of soluble collagen after sterilization (Figure 23B), no statistically significant differences were discovered among all the samples. Nevertheless, the cubic-shaped sample appeared to present more reduction in soluble collagen content, from 5.40 ± 1.53 ug/mg (PV4_CUBE) decreased to 2.62 ± 0.74 ug/mg (PV4_CUBE-Sterilized). On the other hand, the PV4_SLICE sample demonstrated slight decrease from 1.74 ± 0.84 ug/mg to 1.35 ± 0.25 ug/mg (PV4_SLICE-Sterilized) after sterilization.

In terms of insoluble collagen content (Figure 23C), after sterilization, the PV4_CUBE sample demonstrated an unexpected increased content from 163.80 ± 69.65 ug/mg to 254.94 ± 55.78 µg/mg (PV4_CUBE-Sterilized). This observed increase in the cubic-shaped sample is biologically implausible, which is likely a consequence of intrinsic heterogeneity within the meniscal matrix, resulting in uneven collagen distribution between tissue subsamples. Conversely, the PV4_SLICE sample exhibited a slightly reduced level from 214.62 ± 53.85 ug/mg to 199.61 ± 41.81 µg/mg, corresponding to the PV4_SLICE-Sterilized sample. However, no significant differences were observed, suggesting that sterilization did not influence the overall preservation of collagen in meniscal tissues obtained from PV4 in the absence of ethanol.

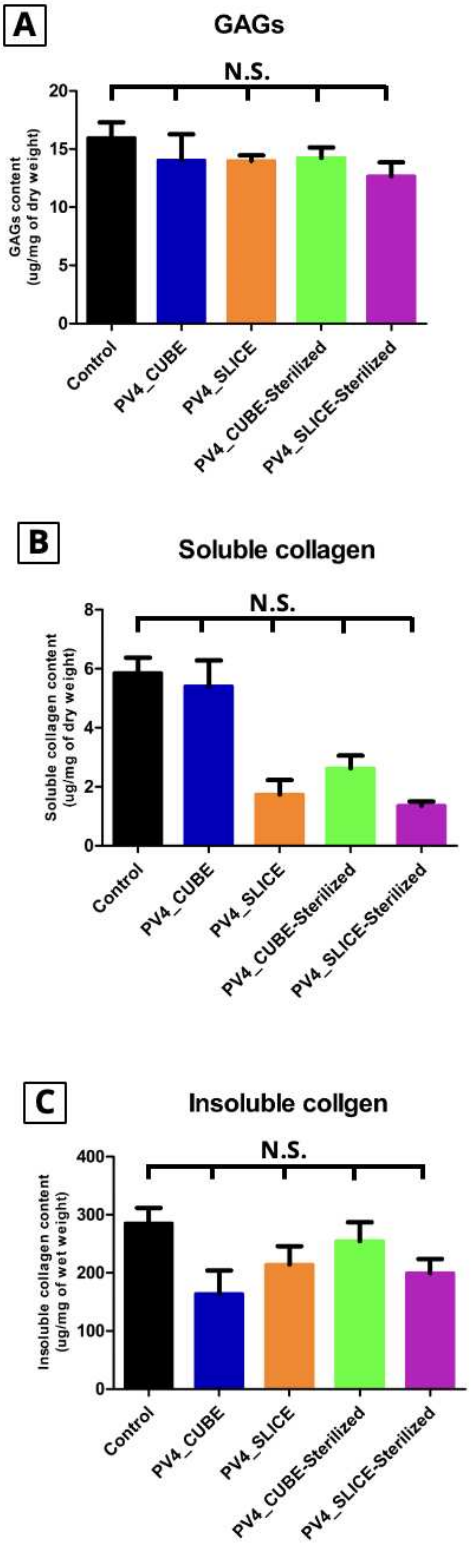

Figure 24 – Quantification of (A) GAGs, (B) soluble collagen, and (C) insoluble collagen content in PV4 before and after sterilization when the application of ethanol as co-solvent was absence.

Regarding the FTIR spectral analysis following sterilization in PV4 (Figure 25), both the Amide I and II band intensities slightly decreased in the PV4_CUBE-Sterilized sample. In the

PV4_SLICE-Sterilized sample, the Amide II band intensity increased and shifted to a higher wavenumber, while the peak at 1450 cm^{-1} decreased. Despite these variations in peak intensities among the different samples, the overall spectral patterns and trends remained largely unchanged.

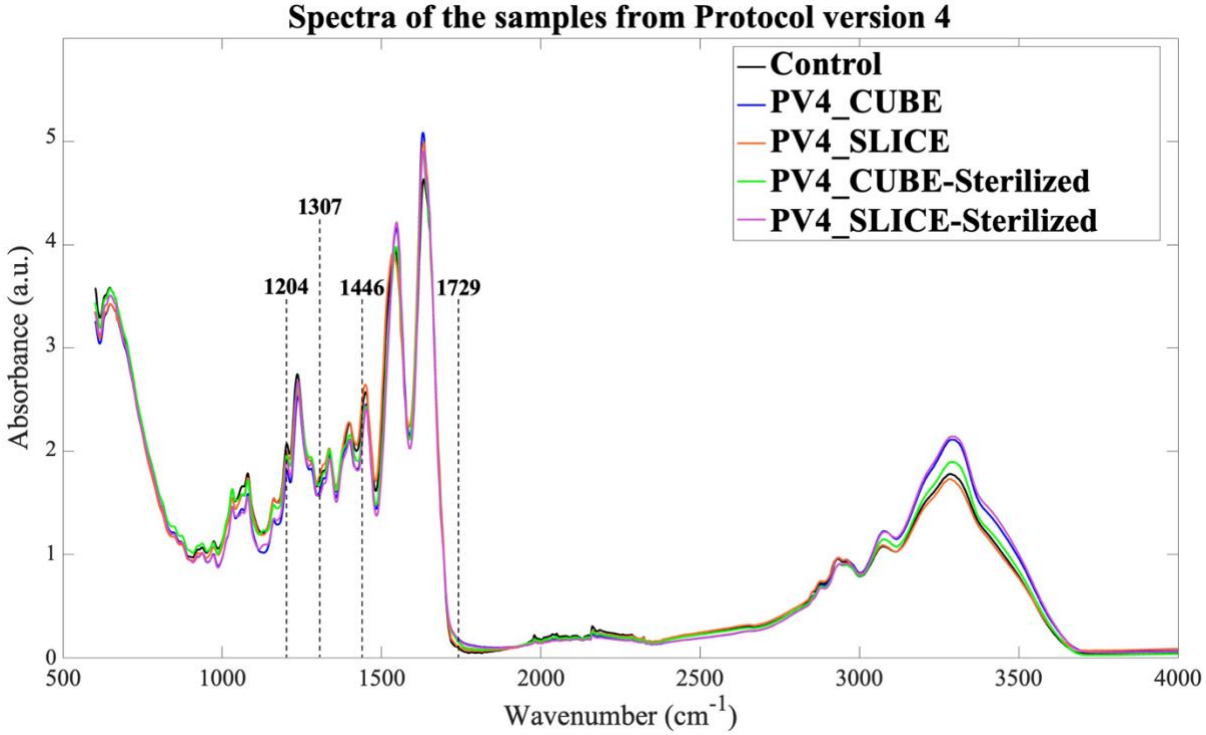

Figure 25 – Spectral profiles of the samples from PV4 before and after sterilization when ethanol was absent, with annotations of unique wavenumbers.

With respect to the PCA analysis of the FTIR spectra (Figure 26), it demonstrates that the majority of spectral variance is explained by PC1, accounting for 91.78% of the total variance. This indicates that the matrix composition of the PV4_SLICE sample was notably affected by the sterilization process. Specifically, the PV4_SLICE sample is located on the positive side of PC1, whereas the sterilized counterpart (PV4_SLICE-Sterilized) shifts to the negative side. In contrast, both cubic samples—before (PV4_CUBE) and after sterilization (PV4_CUBE-Sterilized)—are positioned near the zero axis and within the same region along PC1. Moreover, they are both located in the same side of PC2, which accounts for 4.51% of the spectral variance. These suggest that sterilization had minimal impact on the biomolecular arrangement and conformational alteration of the ECM components in the cubic-shaped sample in PV4 when ethanol was absent.

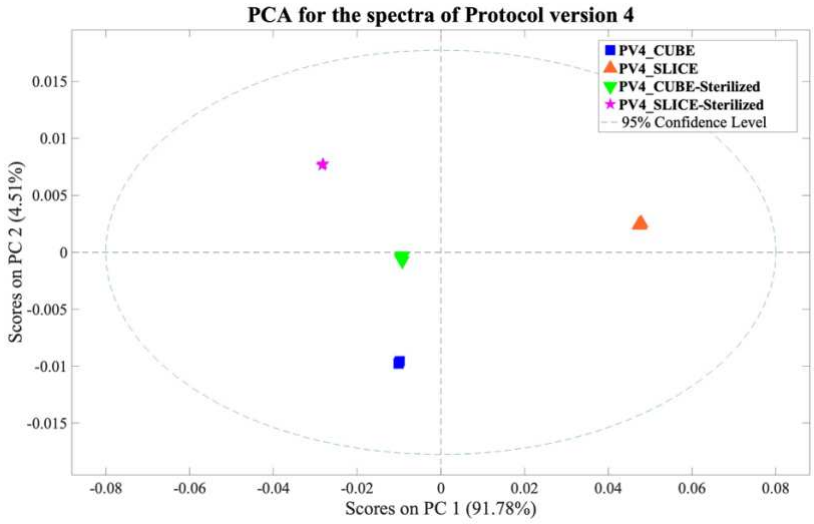

Figure 26 – PCA score plot of the FTIR spectra obtained from PV4 before and after sterilization when ethanol was absent.

Afterwards, loading plot attending to PC1 (Figure 27), which explains the majority of spectral variance, was established to analyze the corresponding molecular features captured by this principal component (Table 11). It reveals that the amide I band, indicative of secondary structure of collagen, is more prominent on the positive side of PC1 and thus more associated with the unsterilized PV4_SLICE sample. Although amide II and III bands are present on both sides of PC1—implying their relative abundance remains consistent across groups—potential conformational alterations may still be inferred from subtle shifts in peak positions.

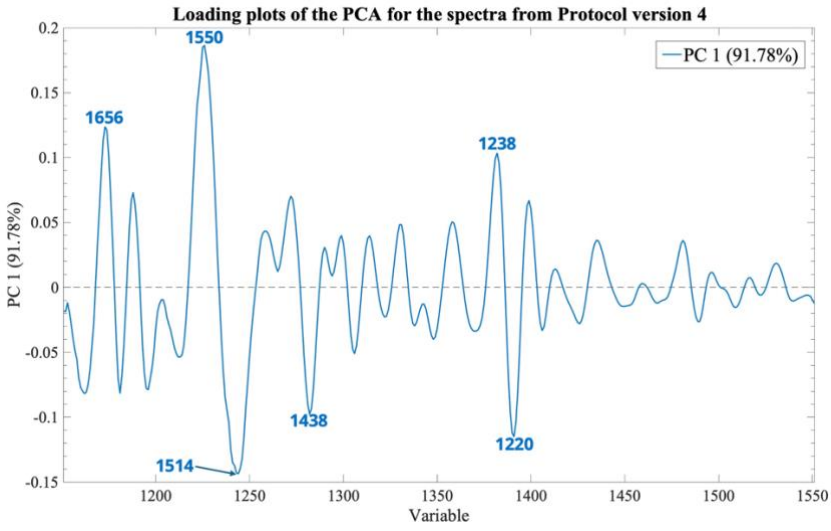

Figure 27 – Loading plot of PC1 from the PCA for PV4 before and after sterilization when ethanol was absent, highlighting the key wavenumbers contributing to the principal component separation.

Table 11 – Peak band assignments corresponding to the major spectral features contributing to PC1 in the PCA of PV4 before and after sterilization when ethanol was absent.

Side of PC1	Peak position (cm^{-1})	Functional group vibrations	Corresponding biomolecules
Positive	1656	Amide I band	Collagen & Elastin
	1550	Amide II band	Collagen
		Uronic acid	GAGs
	1238	Amide III band	Collagen
		SO_3^- sulfated GAGs	GAGs
		Phosphate backbone	Genetic materials
Negative	1514	Amide II band	Collagen
		Uronic acid	GAGs
	1438	Uronic acid	GAGs
	1220	Amide III band	Collagen
		SO_3^- sulfated GAGs	GAGs
		Phosphate backbone	Genetic materials

4. Discussion

The generation of a highly preserved porcine meniscus ECM provides a promising foundation for the development of tissue-engineered strategies for meniscus applications. Four protocol versions were systematically developed to optimize $scCO_2$-assisted approaches, addressing parameters including the number of cycles, depressurization speed, operational pressure, duration per cycle, co-solvent incorporation, as well as washing strategies involving different solvents, washing modes, and physical interventions.

An increase in the number of $scCO_2$ cycles was demonstrated to improve decellularization efficiency, likely attributed to the dynamic nature of pressurization–depressurization pattern that introduces mechanical stress, facilitating membrane disruption and promoting the release of intracellular contents (Zihna *et al.*, 2025; Duarte *et al.*, 2021). Additionally, two depressurization strategies were compared, playing critical roles in influencing decellularization and ECM preservation. Rapid depressurization appeared to enhance a more efficient cellular fragment removal (Guler *et al.*, 2017; Antons *et al.*, 2018), yet it also triggered gas bubble nucleation and phase separation, akin to $scCO_2$ foaming phenomena, where a sudden pressure drop causes the formation of CO_2 crystals or microbubbles within the interstitial spaces in the tissue matrix (Li *et al.*, 2023; Montes *et al.*, 2020). In contrast, slow depressurization enabled gradual release of pressure and gentle diffusion, thereby aiding the removal of cellular components while minimizing mechanical stress on the ECM (Duarte *et al.*, 2021; Durço *et al.*, 2024). Furthermore, different pressures were examined, based on evidence that higher pressure is generally associated with enhanced diffusivity and solvent capacity of supercritical fluids, which could further contribute to the removal of intracellular materials (Lv *et al.*, 2019; López-Padilla *et al.*, 2016). Prolonged exposure time is also expected to increase fluid–tissue interaction, supporting more complete decellularization, particularly in regions with limited accessibility. Previously reported studies supported the relevance of employing elevated pressure and extended treatment times in the $scCO_2$ reactor facilitated the removal of nuclear material from menisci and other cartilaginous tissues with minimal collagen degradation. However, preservation of GAGs remains a critical challenge (Porzucek *et al.*, 2024; Zihna *et al.*, 2025; Anton *et al.*, 2018; Sevastianov *et al.*, 2023). Additionally, given the limited extraction efficiency of $scCO_2$ in polar molecules such as DNA, co-solvents capable of dissolving phospholipids, nucleic acids, and cellular proteins, are often incorporated (Porzucek *et al.*, 2024; Huang *et al.*, 2013). Ethanol as a co-solvent has been demonstrated promising outcomes in enhancing decellularization efficiency by increasing the polarity of $scCO_2$ and

promoting solubilization of hydrophilic cell membrane and nuclear material (Gil-Ramírez *et al.*, 2019; Vernice *et al.*, 2022).

During the $scCO_2$ cyclic treatment, several approaches regarding intermediate washing and physical interventions were employed, intending to enhance the decellularization efficiency. The washing steps combined UPW, hypotonic relative to cellular contents to facilitate water influx, followed by PBS, which is mildly hypertonic and supports the removal of cellular and nucleic acids (Neishabouri *et al.*, 2022). This osmotic stress environment promotes cell swelling and eventual membrane rupture for the clearance of intracellular contents (McInnes *et al.*, 2022). Concerning physical interventions, freeze–thaw induces the formation and expansion of intracellular ice crystals and subsequently the contraction and melting of these crystals to exert mechanical stress on cellular membranes, which has been widely adopted as a supplementary pre-treatment in meniscal decellularization protocols (Zihna *et al.*, 2025; Kim *et al.*, 2020; Kara *et al.*, 2021). In addition, direct ultrasonication produces focused acoustic cavitation to promote more effective mechanical permeabilization, enhancing the rupture of residual intracellular contents (Moffat *et al.*, 2022; Forouzesh *et al.*, 2019; Mardhiyah *et al.*, 2017). Furthermore, Gupt *et al.* (2024) demonstrated that lyophilization caused significant biochemical and morphological damage to cells, contributing to a reduction in graft antigenicity, thereby emerging as a valuable supplementary treatment in decellularization workflows (Porzucek *et al.*, 2024; Butler *et al.*, 2017; Batioglu-Karaaltin *et al.*, 2019).

In this work, a cyclic $scCO_2$-assisted protocol was demonstrated to be efficient in decellularizing porcine meniscus, as evidenced by the progressive reduction in DNA content with an increasing number of $scCO_2$ cycles, consistent with previous finding (Zihna *et al.*, 2025). Additionally, slow depressurization was shown to be critical for effective decellularization, as tighter nucleic acid packaging was detected only via FTIR-derived chemometric analysis when rapid depressurization was employed. This phenomenon is likely related to the more aggressive dehydration typically induced by rapid depressurization, wherein the instantaneous phase transition of $scCO_2$ into gaseous CO_2 diminishes its capacity to retain water and other solubilized substances (Quinn *et al.*, 2022; Pravallika *et al.*, 2023; Yang *et al.*, 2020). With the nature of porcine meniscal matrix being dense and avascular, fluid penetration is inherently restricted, and the presence of compacted and hydrophilic nucleic acid packaging further restricts $scCO_2$ accessibility and its ability to extract genetic material (Porzucek *et al.*, 2024; Antons *et al.*, 2018; Gil-Ramirez *et al.*, 2020). Moreover, the generation of crystalline structures may occlude microchannels and interfibrillar spaces, potentially hindering the removal of genetic debris. Consequently, slow depressurization is considered beneficial, facilitating more

effective removal of residual DNA through gradual CO_2 diffusion while preserving matrix integrity, in line with the literature (de Souza *et al.*, 2025).

In contrast, increasing pressure, extending duration in the $scCO_2$ reactor, or altering sample architecture did not yield significant improvements in decellularization efficiency. This suggests that the diffusional capacity of $scCO_2$ within the porcine meniscus may have reached a saturation point. In this stage, although the supercritical fluid likely permeates the matrix homogeneously, further improvements in DNA removal are constrained, likely due to limited accessibility to deeply embedded or matrix-bound DNA. Additionally, the inclusion of ethanol as a co-solvent was found to impair decellularization efficacy, contrary to the prevailing consensus that ethanol enhances this process. A plausible explanation for this discrepancy is the excessive matrix dehydration caused by high ethanol concentrations, which may reduce tissue porosity and hinder $scCO_2$ diffusion (Durço *et al.*, 2024). These findings imply a threshold in the decellularization efficiency of porcine meniscus achievable by the exclusive application of $scCO_2$ fluid. Furthermore, the employing of detergent during intermediate washing and physical interventions did not significantly improve decellularization efficiency. Nevertheless, further studies evaluating the independent effects of each physical intervention on decellularization efficiency remain necessary and valuable. Notably, several advantages associated with post-transplantation outcomes have been reported. Chen *et al.* (2024) identified freeze–thawed menisci as the most widely used grafts in allogenic meniscal transplantation and promising candidates for xenografts, due to their ability to mitigate anti-porcine immune responses by attenuating T-cell activation post-implantation. Additionally, lyophilization has been reported to selectively alter specific surface receptors on cells, potentially modifying cellular functions and modulating host immune recognition (Chen *et al.*, 2017). Thus, while these interventions may not directly enhance decellularization, they may offer benefits in modulating immunogenic responses following transplantation.

Beyond decellularization efficiency, ECM preservation was a critical parameter. In meniscus, GAGs support hydration and biomechanical integrity to enhance compressive resistance and promote joint stability, as well as form conjugates with adjacent proteins to foster chondrogenic differentiation of mesenchymal stem cells (MSCs) (Sanchez-Adams et al., 2011; Wang et al., 2017). Animal-derived collagen, broadly categorized into soluble and insoluble forms—with the latter predominating in porcine meniscus tissue—retains the triple-helical structure, yet insoluble collagen exhibits significantly higher crosslinking capacity due to its assembly into mature, water-insoluble fibrils (Martínez-Puig *et al.*, 2023; Ghodbane *et al.*, 2016). Quantification of GAGs, soluble collagen, and insoluble collagen confirmed the capacity of the

developed detergent-free $scCO_2$-assisted protocol to preserve ECM components. Furthermore, comparative analysis of PCA plots from ethanol-free and ethanol-treated samples indicated that ethanol inclusion induced more pronounced alterations in ECM composition, particularly in the collagen network. In ethanol-treated samples, shifts in dominant amide band expressions relative to controls suggested partial denaturation of the native triple-helical collagen conformation, leading to reduced expression of the triple-helix by amide I band and enhanced detection of broader secondary structures by amide II band (Sukumaran *et al.*, 2017). This was further supported by a decreased peak ratio between the amide III band and the 1450 cm^{-1} band, a known marker of triple-helix disruption (Xu *et al.*, 2023; Li *et al.*, 2024). Such collagen denaturation under high ethanol concentrations in $scCO_2$ has been previously reported, potentially attributed to disruption of hydrogen bonds and removal of essential water molecules (de Souza *et al.*, 2025; Xu *et al.*, 2021). Nonetheless, both ethanol-free and ethanol-treated groups exhibited reduced FTIR absorbance in the 700–1135 cm^{-1} spectral region, which has been correlated with the degradation of chondroitin sulfate, a key GAG contributing to meniscal biomechanical integrity (Sanchez-Adams *et al.*, 2011; Vidal *et al.*, 2016). As this spectral reduction was absent in previous protocols, the observed GAG degradation may be attributed to the higher operational pressures and prolonged exposure times employed, lining up with previous findings (Zihna et al., 2025; Durço et al., 2024). Moreover, altered spectral features in the ethanol-treated samples within the same region suggest possible retention of residual ethanol, due to interference from its C–O stretching vibrations (Doroshenko *et al.*, 2013).

Sterilization of decellularized biomaterials is essential for clinical translation. Delgado *et al.* (2014) reported that conventional sterilization methods—including ethylene oxide, γ-irradiation, e-beam irradiation, and gas plasma—induced significant mechanical degradation, collagen chain cleavage, and raised cytotoxicity concerns in collagen-based devices. As an alternative, $scCO_2$ sterilization with the additive NovaKill™ has gained attention and has been extensively investigated across various tissue types (O'Connell *et al.*, 2025; Shin *et al.*, 2024; Farey *et al.*, 2024). NovaKill™ comprises a mixture of PAA and H_2O_2, both of which exhibit potent oxidative properties capable of inducing cell death across a broad spectrum of microorganisms (Matuska *et al.*, 2015). Biochemical assay results demonstrated ECM preservation as no significant reduction was observed after sterilization. However, the sterilization induced more pronounced ECM conformational alterations in samples sectioned in slice. Specifically, the collagen network of the sliced-shaped sample appeared more affected, as evidenced by the absence of amide I band feature, suggesting disruption of the ordered molecular packing of collagen fibrils. This observation aligns with reports that PAA-based

sterilization can loosen collagen fibril networks (Delgado *et al.*, 2014). Following sterilization, an additional $scCO_2$ cycle followed by a two-day placement in a flow chamber appeared to be effective in eliminating residual NovaKill™ from the matrices. This was suggested by the absence of characteristic absorption bands at ~1204 cm^{-1}, ~1446 cm^{-1}, and ~1729 cm^{-1} (corresponding to C–O–O bending, C–O stretching, and C=O stretching of PAA, respectively), and ~1307 cm^{-1} (associated with O–H bending of H_2O_2) (Fu *et al.*, 2023).

Collectively, the developed detergent-free $scCO_2$-assisted decellularization protocol achieved substantial DNA reduction in porcine meniscus while preserving ECM components with only moderate degradation. Although the established decellularization threshold was not fully met, adherence to such quantitative standards does not guarantee absence of post-implantation complications (de Figueiredo *et al.*, 2023; Samson *et al.*, 2021). Crucially, recent findings by Cheng *et al.* (2025) emphasize that residual endotoxins—rather than DNA—are critical determinants of host response and regenerative outcomes, emphasizing the need to prioritize such optimization parameters targeting endotoxin removal in future protocol development.

5. Conclusion

In this study, a detergent-free, cyclic $scCO_2$-assisted decellularization protocol was systematically developed and optimized for porcine meniscal tissues, intending to manufacture biologically functional scaffolds for orthopedic applications in tissue engineering, transplantation, and regenerative medicine. Four distinct $scCO_2$-assisted protocols were evaluated. Particularly, a total nine cycles of $scCO_2$ treatment conducted with slow depressurization in the absence of ethanol co-solvent effectively enhances cellular removal from porcine meniscus tissue while preserving critical ECM components, although modest structural degradation with respect to GAGs integrity was suggested. Subsequently, sterilization using $scCO_2$ in combination with NovaKill™ further validated the clinical translatability of the dECM, wherein FTIR spectral analysis confirmed the absence of residual sterilants inside the matrices. Moreover, ECM quantifications post-sterilization indicated minimal biochemical compromise while FTIR analysis revealed that the ECM integrity of the sample sectioned in cube appear to be pronounced preserved after sterilization.

Collectively, these findings demonstrated that $scCO_2$-assisted decellularization offers an effective, time saving, chemical-mild, and environmentally sustainable approach to produce structurally and biochemically preserved meniscal dECM. The resulting matrix exhibits promising attributes for future applications in orthopedic applications and regenerative therapies.

6. Future directions

Building upon the findings of this study, several future directions are proposed to further advance the developed protocol and expand its translational potential. Upcoming work may include the assessment of sterilization efficiency, quantification of endotoxin, and *in vitro* cell culture experiments to assess the immuno- and inflammatory responses of the sterilized scaffolds.

In parallel, to broaden the scope of application, the decellularization porcine meniscus ECM will be explored as a raw material for hydrogel formulation. These ECM-derived hydrogels could serve as injectable scaffolds or be adapted for use in 3D bioprinting applications as bioinks. These bioinks are expected to enable the fabrication of customizable, patient-specific scaffolds for meniscal regeneration.

7. References

Wu, J., Xu, J., Huang, Y., Tang, L., & Hong, Y. (2021). Regional-specific meniscal extracellular matrix hydrogels and their effects on cell–matrix interactions of fibrochondrocytes. *Biomedical Materials*, *17*(1), 014105.

Bian, Y., Cai, X., Wang, H., Xu, Y., Lv, Z., Feng, B., & Weng, X. (2024). Short-term but not long-term knee symptoms and functional improvements of tissue engineering strategy for meniscus defects: a systematic review of clinical studies. *Arthroscopy: The Journal of Arthroscopic & Related Surgery*, *40*(3), 983-995.

Bian, Y., Cai, X., Zhou, R., Lv, Z., Xu, Y., Wang, Y., ... & Weng, X. (2025). Advances in meniscus tissue engineering: Towards bridging the gaps from bench to bedside. *Biomaterials*, *312*, 122716.

Bian, Y., Wang, H., Zhao, X., & Weng, X. (2022). Meniscus repair: up-to-date advances in stem cell-based therapy. *Stem cell research & therapy*, *13*(1), 207.

Murphy, C. A., Cunniffe, G. M., Garg, A. K., & Collins, M. N. (2019). Regional dependency of bovine meniscus biomechanics on the internal structure and glycosaminoglycan content. *Journal of the mechanical behavior of biomedical materials*, *94*, 186-192.

Murphy, C. A., Garg, A. K., Silva-Correia, J., Reis, R. L., Oliveira, J. M., & Collins, M. N. (2019). The meniscus in normal and osteoarthritic tissues: facing the structure property challenges and current treatment trends. *Annual review of biomedical engineering*, *21*(1), 495-521.

Kwon, H., Brown, W. E., Lee, C. A., Wang, D., Paschos, N., Hu, J. C., & Athanasiou, K. A. (2019). Surgical and tissue engineering strategies for articular cartilage and meniscus repair. *Nature Reviews Rheumatology*, *15*(9), 550-570.

Berni, Matteo, et al. "Anisotropy and inhomogeneity of permeability and fibrous network response in the pars intermedia of the human lateral meniscus." *Acta biomaterialia* 135 (2021): 393-402.

Porzucek, F., Mankowska, M., Semba, J. A., Cywoniuk, P., Augustyniak, A., Mleczko, A. M., ... & Rybka, J. D. (2024). Development of a porcine decellularized extracellular matrix (DECM) bioink for 3D bioprinting of meniscus tissue engineering: formulation, characterisation and biological evaluation. *Virtual and Physical Prototyping*, *19*(1), e2359620.

Karjalainen, V. P., Herrera Millar, V. R., Modina, S., Peretti, G. M., Pallaoro, M., Elkhouly, K., ... & Finnilä, M. A. (2024). Age and anatomical region-related differences in vascularization of the porcine meniscus using microcomputed tomography imaging. *Journal of Orthopaedic Research®*, *42*(9), 2095-2105.

Suzuki, S., Mizuno, M., Sakamaki, Y., Mimata, A., Endo, K., Kohno, Y., ... & Sekiya, I. (2020). Morphological changes in synovial mesenchymal stem cells during their adhesion to the meniscus. *Laboratory Investigation*, *100*(7), 916-927.

Jacob, G., Shimomura, K., Krych, A. J., & Nakamura, N. (2019). The meniscus tear: a review of stem cell therapies. *Cells*, *9*(1), 92.

Chen, M., Guo, W., Gao, S., Hao, C., Shen, S., Zhang, Z., ... & Guo, Q. (2018). Biomechanical stimulus based strategies for meniscus tissue engineering and regeneration. *Tissue Engineering Part B: Reviews*, *24*(5), 392-402.

Gonzalez-Leon, Erik A., Jerry C. Hu, and Kyriacos A. Athanasiou. "Yucatan minipig knee meniscus regional biomechanics and biochemical structure support its suitability as a large

animal model for translational research." *Frontiers in Bioengineering and Biotechnology* 10 (2022): 844416.

He, Yong, et al. "Preparation and characterization of an optimized meniscal extracellular matrix scaffold for meniscus transplantation." *Frontiers in Bioengineering and Biotechnology* 8 (2020): 779.

Fischer, D. C., Sckell, A., Garkisch, A., Dresing, K., Eisenhauer, A., Valentini, L., & Mittlmeier, T. (2021). Treatment of perioperative swelling by rest, ice, compression, and elevation (RICE) without and with additional application of negative pressure (RICE+) in patients with a unilateral ankle fracture: study protocol for a monocentric, evaluator-blinded randomized controlled pilot trial. *Pilot and Feasibility Studies*, 7, 1-9.

Lim, W. B., & Al-Dadah, O. (2022). Conservative treatment of knee osteoarthritis: A review of the literature. *World journal of orthopedics*, *13*(3), 212.

Yeo, D. Y., Suhaimi, F., & Parker, D. A. (2019). Factors predicting failure rates and patient-reported outcome measures after arthroscopic meniscal repair. *Arthroscopy: The Journal of Arthroscopic & Related Surgery*, *35*(11), 3146-3164.

Otsuki, S., Sezaki, S., Okamoto, Y., Ishitani, T., Wakama, H., & Neo, M. (2024). Safety and efficacy of a novel polyglycolic acid meniscal scaffold for irreparable meniscal tear. *Cartilage*, *15*(2), 110-119.

Jian, Z., Zhuang, T., Qinyu, T., Liqing, P., Kun, L., Xujiang, L., ... & Quanyi, G. (2021). 3D bioprinting of a biomimetic meniscal scaffold for application in tissue engineering. *Bioactive materials*, *6*(6), 1711-1726.

Abpeikar, Z., Javdani, M., Alizadeh, A., Khosravian, P., Tayebi, L., & Asadpour, S. (2022). Development of meniscus cartilage using polycaprolactone and decellularized meniscus surface modified by gelatin, hyaluronic acid biomacromolecules: a rabbit model. *International journal of biological macromolecules*, *213*, 498-515.

Li, H., Li, P., Yang, Z., Gao, C., Fu, L., Liao, Z., ... & Guo, Q. (2021). Meniscal regenerative scaffolds based on biopolymers and polymers: recent status and applications. *Frontiers in Cell and Developmental Biology*, *9*, 661802.

Guo, W., Chen, M., Wang, Z., Tian, Y., Zheng, J., Gao, S., ... & Guo, Q. (2021). 3D-printed cell-free PCL–MECM scaffold with biomimetic micro-structure and micro-environment to enhance in situ meniscus regeneration. *Bioactive Materials*, *6*(10), 3620-3633.

Kim, J. A., An, Y. H., Yim, H. G., Han, W. J., Park, Y. B., Park, H. J., ... & Ha, C. W. (2021). Injectable fibrin/polyethylene oxide semi-IPN hydrogel for a segmental meniscal defect regeneration. *The American Journal of Sports Medicine*, *49*(6), 1538-1550.

Vadodaria, K., Kulkarni, A., Santhini, E., & Vasudevan, P. (2019). Materials and structures used in meniscus repair and regeneration: a review. *Biomedicine*, *9*(1), 2.

Wu, J., Ding, Q., Dutta, A., Wang, Y., Huang, Y. H., Weng, H., ... & Hong, Y. (2015). An injectable extracellular matrix derived hydrogel for meniscus repair and regeneration. *Acta biomaterialia*, *16*, 49-59.

Takroni, T., Laouar, L., Adesida, A., Elliott, J. A., & Jomha, N. M. (2016). Anatomical study: comparing the human, sheep and pig knee meniscus. *Journal of experimental orthopaedics*, *3*, 1-13.

Fischenich, K. M., Boncella, K., Lewis, J. T., Bailey, T. S., & Haut Donahue, T. L. (2017). Dynamic compression of human and ovine meniscal tissue compared with a potential

thermoplastic elastomer hydrogel replacement. *Journal of Biomedical Materials Research Part A*, *105*(10), 2722-2728.

Di Giancamillo, A., Deponti, D., Addis, A., Domeneghini, C., & Peretti, G. M. (2014). Meniscus maturation in the swine model: changes occurring along with anterior to posterior and medial to lateral aspect during growth. *Journal of cellular and molecular medicine*, *18*(10), 1964-1974.

Chen, R., Zhao, H., Ai, L., Zhang, J., & Jiang, D. (2024). Inhibiting T-cell-mediated rejection of the porcine meniscus through freeze-thawing and downregulating porcine xenoreactive antigen genes. *Cell Transplantation*, *33*, 09636897241273689.

Mazy, D., Lu, D., Leclerc, S., Laor, B., Wang, J., Pinvicy, A., ... & Nault, M. L. (2024). Animal models used in meniscal repair research from ex vivo to in vivo: A systematic review. *Journal of Orthopaedics*.

Han, P. F., Zhang, R., Gao, Y. Y., Li, P. C., Wei, X. C., & Lv, Z. (2020). Establishment and simulation of 3D geometric models of mini-pig and sheep knee joints using finite element analysis. *Medical Science Monitor: International Medical Journal of Experimental and Clinical Research*, *26*, e921540-1.

Golebiowska, A. A., Intravaia, J. T., Sathe, V. M., Kumbar, S. G., & Nukavarapu, S. P. (2024). Decellularized extracellular matrix biomaterials for regenerative therapies: advances, challenges and clinical prospects. *Bioactive Materials*, *32*, 98-123.

McCrary, M. W., Bousalis, D., Mobini, S., Song, Y. H., & Schmidt, C. E. (2020). Decellularized tissues as platforms for in vitro modeling of healthy and diseased tissues. *Acta biomaterialia*, *111*, 1-19.

Dehghani, S., Aghaee, Z., Soleymani, S., Tafazoli, M., Ghabool, Y., & Tavassoli, A. (2024). An overview of the production of tissue extracellular matrix and decellularization process. *Cell and Tissue Banking*, *25*(1), 369-387.

2015 Clinical Evaluation of dCELL® Meniscus for Partial Replacement of the Meniscus (Bethesda, MD: National Institutes of Health) (ClinicalTrials.gov Identifier: NCT02270905) Available: https://clinicaltrials.gov/ct2/show/NCT02270905 [Visited date: 30/05/25]

Parmaksiz, M., Dogan, A., Odabas, S., Elçin, A. E., & Elçin, Y. M. (2016). Clinical applications of decellularized extracellular matrices for tissue engineering and regenerative medicine. *Biomedical materials*, *11*(2), 022003.

Ding, Y., Zhang, W., Sun, B., Mo, X., & Wu, J. (2022). Cyclic freeze–thaw grinding to decellularize meniscus for fabricating porous, elastic scaffolds. *Journal of Biomedical Materials Research Part A*, *110*(11), 1824-1839.

Li, Z., Yan, W., Zhao, F., Wang, H., Cheng, J., Duan, X., ... & Ao, Y. (2023). Regional specific tunable meniscus decellularized extracellular matrix (MdECM) reinforced bioink promotes anistropic meniscus regeneration. *Chemical Engineering Journal*, *473*, 145209.

White, L. J., Taylor, A. J., Faulk, D. M., Keane, T. J., Saldin, L. T., Reing, J. E., ... & Badylak, S. F. (2017). The impact of detergents on the tissue decellularization process: a ToF-SIMS study. *Acta biomaterialia*, *50*, 207-219.

Fernández-Pérez, J., & Ahearne, M. (2019). The impact of decellularization methods on extracellular matrix derived hydrogels. *Scientific reports*, *9*(1), 14933.

Cebotari, S., Tudorache, I., Jaekel, T., Hilfiker, A., Dorfman, S., Ternes, W., ... & Lichtenberg, A. (2010). Detergent decellularization of heart valves for tissue engineering: toxicological effects of residual detergents on human endothelial cells. *Artificial organs*, *34*(3), 206-210.

Mendibil, U., Ruiz-Hernandez, R., Retegi-Carrion, S., Garcia-Urquia, N., Olalde-Graells, B., & Abarrategi, A. (2020). Tissue-specific decellularization methods: rationale and strategies to achieve regenerative compounds. *International journal of molecular sciences*, *21*(15), 5447.

Topuz, B., Günal, G., Guler, S., & Aydin, H. M. (2020). Use of supercritical CO2 in soft tissue decellularization. In *Methods in cell biology* (Vol. 157, pp. 49-79). Academic Press.

Kim, B. S., Kim, J. U., So, K. H., & Hwang, N. S. (2021). Supercritical fluid-based decellularization technologies for regenerative medicine applications. *Macromolecular Bioscience*, *21*(8), 2100160.

Okolie, J. A., Nanda, S., Dalai, A. K., & Kozinski, J. A. (2022). Advances in the industrial applications of supercritical carbon dioxide. In *Carbon Dioxide Capture and Conversion* (pp. 237-256). Elsevier.

Bernhardt, A., Wehrl, M., Paul, B., Hochmuth, T., Schumacher, M., Schütz, K., & Gelinsky, M. (2015). Improved sterilization of sensitive biomaterials with supercritical carbon dioxide at low temperature. *PloS one*, *10*(6), e0129205.

Bento, C. S., Alarico, S., Empadinhas, N., de Sousa, H. C., & Braga, M. E. (2022). Sequential scCO2 drying and sterilisation of alginate-gelatine aerogels for biomedical applications. *The Journal of Supercritical Fluids*, *184*, 105570.

Montalbán, M. G., & Víllora, G. (2022). *Phase Equilibria With Supercritical Carbon Dioxide-Application to the Components of a Biocatalytic Process*.

Choi, S. J., Han, J., Shin, Y. H., & Kim, J. K. (2024). Increased efficiency of peripheral nerve regeneration using supercritical carbon dioxide-based decellularization in acellular nerve graft. *Scientific Reports*, *14*(1), 23696.

Ozudogru, E., Kurt, T., Derkus, B., Cengiz, U., & Arslan, Y. E. (2024). Supercritical CO2-Mediated Decellularization of Bovine Spinal Cord Meninges: A Comparative Study for Decellularization Performance. *ACS omega*, *9*(49), 48781-48790.

Zihna, G., Kilic, B., Topuz, B., Gunal, G., & Aydin, H. M. (2025). Comparative analysis of supercritical-based and chemical-based decellularization technique for meniscus tissue. *The Journal of Supercritical Fluids*, *219*, 106518.

Bieberle-Hütter, A., Bronneberg, A. C., George, K., & Van De Sanden, M. C. M. (2021). Operando attenuated total reflection Fourier-transform infrared (ATR-FTIR) spectroscopy for water splitting. *Journal of Physics D: Applied Physics*, *54*(13), 133001.

Campanella, B., Palleschi, V., & Legnaioli, S. (2021). Introduction to vibrational spectroscopies. *ChemTexts*, *7*, 1-21.

Xu, R., Wu, J., Zheng, L., & Zhao, M. (2023). Undenatured type II collagen and its role in improving osteoarthritis. *Ageing research reviews*, *91*, 102080.

Salinas-Fernandez, S., Garcia, O., Kelly, D. J., & Buckley, C. T. (2024). The influence of pH and salt concentration on the microstructure and mechanical properties of meniscus extracellular matrix-derived implants. *Journal of Biomedical Materials Research Part A*, *112*(3), 359-372.

Jeevithan, E., Bao, B., Bu, Y., Zhou, Y., Zhao, Q., & Wu, W. (2014). Type II collagen and gelatin from silvertip shark (Carcharhinus albimarginatus) cartilage: Isolation, purification, physicochemical and antioxidant properties. *Marine Drugs*, *12*(7), 3852-3873.

Li, Y., Zhang, Y., & Zhang, G. (2024). Comparative Analysis of Decellularization Methods for the Production of Decellularized Umbilical Cord Matrix. *Current Issues in Molecular Biology*, *46*(7), 7686-7701.

Brézillon, S., Untereiner, V., Lovergne, L., Tadeo, I., Noguera, R., Maquart, F. X., ... & Sockalingum, G. D. (2014). Glycosaminoglycan profiling in different cell types using infrared spectroscopy and imaging. *Analytical and bioanalytical chemistry*, *406*, 5795-5803.

Popescu, M. C., Vasile, C., & Craciunescu, O. (2010). Structural analysis of some soluble elastins by means of FT-IR and 2D IR correlation spectroscopy. *Biopolymers*, *93*(12), 1072-1084.

Lozano, M., Rodríguez-Ulibarri, P., Echeverría, J. C., Beruete, M., Sorolla, M., & Beriain, M. J. (2017). Mid-infrared spectroscopy (MIR) for simultaneous determination of fat and protein content in meat of several animal species. *Food Analytical Methods*, *10*(10), 3462-3470.

Pachetti, M., Zupin, L., Venturin, I., Mitri, E., Boscolo, R., D'Amico, F., ... & Pascolo, L. (2020). FTIR spectroscopy to reveal lipid and protein changes induced on sperm by capacitation: bases for an improvement of sample selection in ART. *International Journal of Molecular Sciences*, *21*(22), 8659.

van de Voort, F. R., Sedman, J., & Russin, T. (2001). Lipid analysis by vibrational spectroscopy. *European Journal of Lipid Science and Technology*, *103*(12), 815-826.

Froehlich, E., Mandeville, J. S., Weinert, C. M., Kreplak, L., & Tajmir-Riahi, H. A. (2011). Bundling and aggregation of DNA by cationic dendrimers. *Biomacromolecules*, *12*(2), 511-517.

Talari, A. C. S., Martinez, M. A. G., Movasaghi, Z., Rehman, S., & Rehman, I. U. (2017). Advances in Fourier transform infrared (FTIR) spectroscopy of biological tissues. *Applied Spectroscopy Reviews*, *52*(5), 456-506.

Mello, M. L. S., & Vidal, B. C. (2012). Changes in the infrared microspectroscopic characteristics of DNA caused by cationic elements, different base richness and single-stranded form.

Wood, B. R. (2016). The importance of hydration and DNA conformation in interpreting infrared spectra of cells and tissues. *Chemical Society Reviews*, *45*(7), 1980-1998.

Paston, S. V., Polyanichko, A. M., Shulenina, O. V., & Osinnikova, D. N. (2020). A study of the DNA structure in films using FTIR spectroscopy. *Biophysics*, *65*, 900-906.

Mustafa, M., Ali, A., Siddiqui, S. A., Mir, A. R., Kausar, T., Nayeem, S. M., ... & Habib, S. (2022). Biophysical characterization of structural and conformational changes in methylmethane sulfonate modified DNA leading to the frizzled backbone structure and strand breaks in DNA. *Journal of Biomolecular Structure and Dynamics*, *40*(16), 7598-7611.

Bonnet, J., Colotte, M., Coudy, D., Couallier, V., Portier, J., Morin, B., & Tuffet, S. (2010). Chain and conformation stability of solid-state DNA: implications for room temperature storage. *Nucleic acids research*, *38*(5), 1531-1546.

Sumi, H., Ohta, N., Sekiguchi, H., Harada, S., Ujihara, T., Tsukamoto, K., & Tagawa, M. (2021). Two-Step Nanoparticle Crystallization via DNA-Guided Self-Assembly and the Nonequilibrium Dehydration Process. *Crystal Growth & Design*, *21*(8), 4506-4515.

Quinn, D., Stannard, D., Edwards, J., Botros, K. K., & Johansen, C. (2022). Experimental visualization and characteristics of bubble nucleation during rapid decompression of supercritical and subcooled carbon dioxide. *International Journal of Pressure Vessels and Piping*, *195*, 104569.

Vidal, B. D. C., & Mello, M. L. S. (2016). FT-IR microspectroscopy of rat ear cartilage. *PLoS One*, *11*(3), e0151989.

Wang, P., Balko, J., Lu, R., López-Lorente, Á. I., Dürselen, L., & Mizaikoff, B. (2018). Analysis of human menisci degeneration via infrared attenuated total reflection spectroscopy. *Analyst*, *143*(20), 5023-5029.

Belbachir, K., Noreen, R., Gouspillou, G., & Petibois, C. (2009). Collagen types analysis and differentiation by FTIR spectroscopy. *Analytical and bioanalytical chemistry*, *395*, 829-837.

Bryan, M. A., Brauner, J. W., Anderle, G., Flach, C. R., Brodsky, B., & Mendelsohn, R. (2007). FTIR studies of collagen model peptides: complementary experimental and simulation approaches to conformation and unfolding. *Journal of the American Chemical Society*, *129*(25), 7877-7884.

Duarte, M. M., Ribeiro, N., Silva, I. V., Dias, J. R., Alves, N. M., & Oliveira, A. L. (2021). Fast decellularization process using supercritical carbon dioxide for trabecular bone. *The Journal of Supercritical Fluids*, *172*, 105194.

Guler, S., Aslan, B., Hosseinian, P., & Aydin, H. M. (2017). Supercritical carbon dioxide-assisted decellularization of aorta and cornea. *Tissue Engineering Part C: Methods*, *23*(9), 540-547.

Antons, J., Marascio, M. G. M., Aeberhard, P., Weissenberger, G., Hirt-Burri, N., Applegate, L. A., ... & Pioletti, D. (2018). Decellularised tissues obtained by a CO2-philic detergent and supercritical CO2.

Li, W., Gong, Z., Wu, K., Zhao, L., & Hu, D. (2023). Effect of crystalline transformation on supercritical CO2 foaming and cell morphology of isotactic polybutene-1. *Journal of CO2 Utilization*, *74*, 102546.

Montes, A., Pereyra, C., & De La Ossa, E. M. (2020). Foaming+ Impregnation One-Step Process Using Supercritical CO 2. In *Advanced Supercritical Fluids Technologies*. IntechOpen.

Durço, M. G. F., Zuliani, C. C., de Souza, V. M., Teixeira, L. H. C., Coimbra, I. B., e Rosa, P. D. T. V., & Moraes, Â. M. (2024). Supercritical cartilage decellularization: Cosolvent effect on mechanical properties. *The Journal of Supercritical Fluids*, *210*, 106270.

López-Padilla, A., Ruiz-Rodriguez, A., Reglero, G., & Fornari, T. (2016). Study of the diffusion coefficient of solute-type extracts in supercritical carbon dioxide: Volatile oils, fatty acids and fixed oils. *The Journal of Supercritical Fluids*, *109*, 148-156.

Sevastianov, V. I., Basok, Y. B., Grigoriev, A. M., Nemets, E. A., Kirillova, A. D., Kirsanova, L. A., ... & Gautier, S. V. (2023). Decellularization of cartilage microparticles: Effects of temperature, supercritical carbon dioxide and ultrasound on biochemical, mechanical, and biological properties. *Journal of Biomedical Materials Research Part A*, *111*(4), 543-555.

Huang, Z., Li, J. H., Li, H. S., Miao, H., Kawi, S., & Goh, A. H. (2013). Effect of the polar modifiers on supercritical extraction efficiency for template removal from hexagonal mesoporous silica materials: solubility parameter and polarity considerations. *Separation and Purification Technology*, *118*, 120-126.

Gil-Ramírez, A., Spangenberg, A., Spégel, P., & Rodríguez-Meizoso, I. (2019). Pressurized carbon dioxide combined with aqueous ethanol as cosolvent induces efficient delipidation of porcine retina for their use as bioscaffolds. *Journal of CO2 Utilization*, *34*, 700-708.

Vernice, N. A., Shih, S., Askinas, C., Dong, X., Bednarski, D. M., Eisenhut, T., & Spector, J. A. (2022). 90. Sustainable and Efficacious Sterilization and Decellularization of Xenograft Cartilage Using Supercritical Carbon Dioxide. *Plastic and Reconstructive Surgery–Global Open*, *10*(6S), 59.

Neishabouri, A., Soltani Khaboushan, A., Daghigh, F., Kajbafzadeh, A. M., & Majidi Zolbin, M. (2022). Decellularization in tissue engineering and regenerative medicine: evaluation, modification, and application methods. *Frontiers in bioengineering and biotechnology*, *10*, 805299.

McInnes, A. D., Moser, M. A., & Chen, X. (2022). Preparation and use of decellularized extracellular matrix for tissue engineering. *Journal of functional biomaterials*, *13*(4), 240.

Kim, W., Onodera, T., Kondo, E., Terkawi, M. A., Homan, K., Hishimura, R., & Iwasaki, N. (2020). Which contributes to meniscal repair, the synovium or the meniscus? An in vivo rabbit model study with the freeze-thaw method. *The American Journal of Sports Medicine*, *48*(6), 1406-1415.

Kara, A., Koçtürk, S., Bilici, G., & Havitcioglu, H. (2021). Development of biological meniscus scaffold: Decellularization method and recellularization with meniscal cell population derived from mesenchymal stem cells. *Journal of Biomaterials Applications*, *35*(9), 1192-1207.

Moffat, D., Ye, K., & Jin, S. (2022). Decellularization for the retention of tissue niches. *Journal of tissue engineering*, *13*, 20417314221101151.

Forouzesh, F., Rabbani, M., & Bonakdar, S. (2019). A comparison between ultrasonic bath and direct sonicator on osteochondral tissue decellularization. *Journal of Medical Signals & Sensors*, *9*(4), 227-233.

Mardhiyah, A., Sha'ban, M., & Azhim, A. (2017, July). Evaluation of histological and biomechanical properties on engineered meniscus tissues using sonication decellularization. In *2017 39th Annual International Conference of the IEEE Engineering in Medicine and Biology Society (EMBC)* (pp. 2064-2067). IEEE.

Gupt, C., Lamba, A. K., Faraz, F., Tandon, S., Augustine, J., Datta, A., & Dhingra, S. (2024). Histological evaluation of decellularization of freeze dried and chemically treated indigenously prepared bovine pericardium membrane. *Cell and Tissue Banking*, *25*(3), 773-784.

Butler, C. R., Hynds, R. E., Crowley, C., Gowers, K. H., Partington, L., Hamilton, N. J., ... & Janes, S. M. (2017). Vacuum-assisted decellularization: an accelerated protocol to generate tissue-engineered human tracheal scaffolds. *Biomaterials*, *124*, 95-105.

Batioglu-Karaaltin, A., Ovali, E., Karaaltin, M. V., Yener, M., Yılmaz, M., Eyüpoğlu, F., ... & Cansiz, H. (2019). Decellularization of trachea with combined techniques for tissue-engineered trachea transplantation. *Clinical and experimental otorhinolaryngology*, *12*(1), 86-94.

Pravallika, K., Chakraborty, S., & Singhal, R. S. (2023). Supercritical drying of food products: An insightful review. *Journal of Food Engineering*, *343*, 111375.

Yang, L., & Liu, H. (2020). Effect of Supercritical CO2 drying on moisture transfer and wood property of Eucalyptus urophydis. *Forests*, *11*(10), 1115.

Gil-Ramirez, A., Rosmark, O., Spegel, P., Swärd, K., Westergren-Thorsson, G., Larsson-Callerfelt, A. K., & Rodriguez-Meizoso, I. (2020). Pressurized carbon dioxide as a potential tool for decellularization of pulmonary arteries for transplant purposes. *Scientific reports*, *10*(1), 4031.

de Souza, V. M., Zuliani, C. C., da Cunha, J. B., Carron, J., Lima, C. S., Coimbra, I. B., ... & Moraes, Â. M. (2025). Greener Decellularization of Porcine Auricular Cartilage Using Supercritical Technology and Different Pretreatments for Application in Tissue Engineering. *ACS Biomaterials Science & Engineering*.

Chen, Y., Chen, J., Zhang, Z., Lou, K., Zhang, Q., Wang, S., ... & Lin, X. (2017). Current advances in the development of natural meniscus scaffolds: innovative approaches to decellularization and recellularization. *Cell and Tissue Research*, *370*, 41-52.

Sanchez-Adams, J., Willard, V. P., & Athanasiou, K. A. (2011). Regional variation in the mechanical role of knee meniscus glycosaminoglycans. *Journal of applied physiology*, *111*(6), 1590-1596.

Wang, M., Liu, X., Lyu, Z., Gu, H., Li, D., & Chen, H. (2017). Glycosaminoglycans (GAGs) and GAG mimetics regulate the behavior of stem cell differentiation. *Colloids and Surfaces B: Biointerfaces*, *150*, 175-182.

Martínez-Puig, D., Costa-Larrión, E., Rubio-Rodríguez, N., & Gálvez-Martín, P. (2023). Collagen supplementation for joint health: The link between composition and scientific knowledge. *Nutrients*, *15*(6), 1332.

Ghodbane, S. A., & Dunn, M. G. (2016). Physical and mechanical properties of cross-linked type I collagen scaffolds derived from bovine, porcine, and ovine tendons. *Journal of Biomedical Materials Research Part A*, *104*(11), 2685-2692.

Sukumaran, S. (2017). Protein secondary structure elucidation using FTIR spectroscopy. *Thermo Fisher Scientific. Available at*.

Xu, S., Gu, M., Wu, K., & Li, G. (2021). Unraveling the interaction mechanism between collagen and alcohols with different chain lengths and hydroxyl positions. *Colloids and Surfaces B: Biointerfaces*, *199*, 111559.

Doroshenko, I., Pogorelov, V., & Sablinskas, V. (2013). Infrared absorption spectra of monohydric alcohols. *Dataset Papers in Science*, *2013*(1), 329406.

Delgado, L. M., Pandit, A., & Zeugolis, D. I. (2014). Influence of sterilisation methods on collagen-based devices stability and properties. *Expert review of medical devices*, *11*(3), 305-314.

O'Connell, J., Pentakota, K., Villeareal, D., Faz, J., Li, X., Trinh, A., ... & Srinivasan, A. (2025). Development of a sterilization process for amniotic membrane allograft tissue using supercritical carbon dioxide and NovaKill. *Cell and Tissue Banking*, *26*(1), 4.

Shin, M., Pelletier, M. H., Lovric, V., Walsh, W. R., Martens, P. J., Kruzic, J. J., & Gludovatz, B. (2024). Effect of gamma irradiation and supercritical carbon dioxide sterilization with Novakill™ or ethanol on the fracture toughness of cortical bone. *Journal of Biomedical Materials Research Part B: Applied Biomaterials*, *112*(1), e35356.

Farey, J. E., Salmon, L. J., Roe, J. P., Russell, V., Sundaraj, K., & Pinczewski, L. A. (2024). Outcomes of ACL Reconstruction Utilizing Supercritical CO2-Sterilized Allografts. *Orthopaedic Journal of Sports Medicine*, *12*(8), 23259671241254115.

Matuska, A. M., & McFetridge, P. S. (2015). The effect of terminal sterilization on structural and biophysical properties of a decellularized collagen-based scaffold; implications for stem cell adhesion. *Journal of Biomedical Materials Research Part B: Applied Biomaterials*, *103*(2), 397-406.

Fu, C. H., Chen, G. Y., Lin, Y. H., Lin, C. H., Muthiah, B., Kasai, T., ... & Yu, D. E. (2023). Kinetic and equilibrium analysis of peracetic acid formation at 1753 cm− 1 mid-infrared absorption peak using facile attenuated total reflection Fourier transform Infrared technique. *Journal of the Chinese Chemical Society*, *70*(6), 1427-1434.

de Figueiredo, S. M. P., Tastaldi, L., Mao, R. M. D., Lima, D. L., Huang, L. C., & Lu, R. (2023). Biologic versus synthetic mesh in open ventral hernia repair: A systematic review and meta-analysis of randomized controlled trials. *Surgery*, *173*(4), 1001-1007.

Samson, D. J., Gachabayov, M., & Latifi, R. (2021). Biologic Mesh in Surgery: A Comprehensive Review and Meta-Analysis of Selected Outcomes in 51 Studies and 6079 Patients. *World Journal of Surgery*, *45*(12), 3524-3540.

Cheng, W., Huang, Y., Dai, J., Zhao, M., Wang, Y., Turner, N., & Zhang, J. (2025). Endotoxin, not DNA, Determines the Host Response and Tissue Regeneration Behavior of Acellular Biologic Scaffolds. *Acta Biomaterialia*.

8. Appendixes

Appendix A – Schematic representation of the four treated samples in PV1.

Appendix B – Decellularization PV2. Notably, between the last two cycles of $scCO_2$ treatment, meniscal sample was stored at -20ºC following lyophilization.

	Day 1			Day 2			Day 3		
Number of cycle	1	2	3	4	5	6	7	8	9
Conditions in the reactor	**P=120 bar ; T=Below 40ºC ; t=1 hour**								
Treatments after the cycle	**Washing with UPW + CLO**								
Conditions during washing	[3 cycles] 10 mins **sonication** + 50 mins orbital shaker		10 mins **sonication** + Orbital shaker overnight	[3 cycles] 10 mins **sonication** + 50 mins orbital shaker		10 mins **sonication** + Orbital shaker overnight	[3 cycles] 10 mins **sonication** + 50 mins orbital shaker		10 mins **sonication** + 10 mins orbital shaker

Appendix C – Decellularization PV3.

	Day 1		Day 2		Day 3		Day 4		Day 5
Number of cycle	1	2	3	4	5	6	7	8	9
Pre-treatments	**Washing with 10 mins PBS and 20 mins UPW+CLO** OR **Washing with 10 mins PBS and 20 mins EDTA**	----------							**Washing with PBS** + **5 cycles of freeze-thaw**
Conditions in the reactor	**P=120 bar ; T=Below 40ºC ; t=1 hour**								
Treatments after the cycle	**Washing with UPW+CLO, following by washing with PBS** OR **Washing with detergent**								
Conditions during washing	**Each run of washing: 30 mins direct sonication + 5 times agitation in bead mill + Oribital shaker**								
Overnight condition	----------	**Washing with PBS+CLO in orbital shaker** OR **Washing with detergent in orbital shaker**	------	**Washing with PBS+CLO in orbital shaker** OR **Washing with detergent in orbital shaker**	------	**Washing with PBS+CLO in orbital shaker** OR **Washing with detergent in orbital shaker**	------	**Lyophilization**	----------

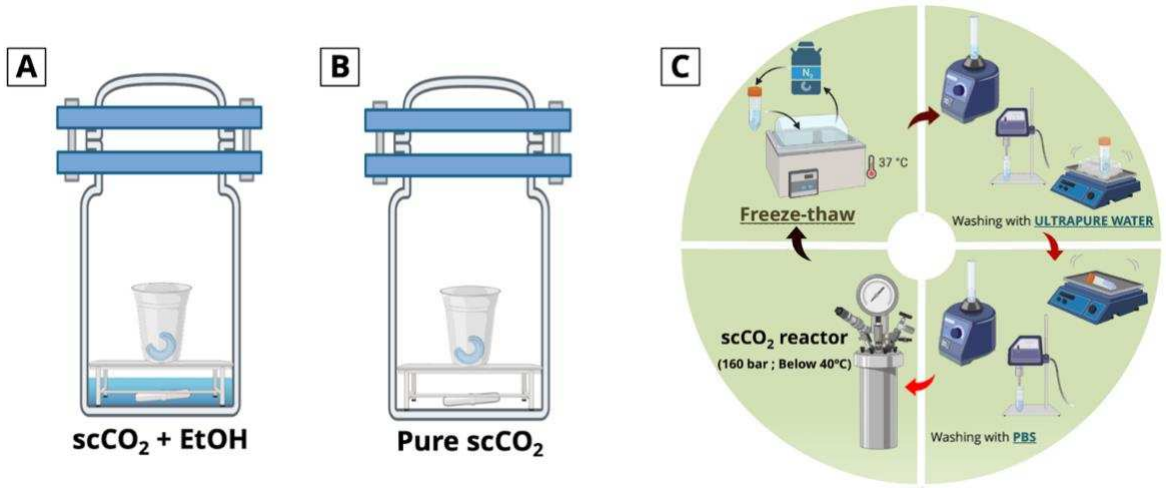

Appendix D – Schematic of meniscus placement in the $scCO_2$ reactor in PV4 (A) with and (B) without EtOH as a co-solvent; (C) Workflow diagram of treatments within each $scCO_2$ cycle for PV4.

Appendix E – Summary of decellularization PV4.

	Day 1		Day 2		Day 3		Day 4		Day 5
Number of cycle	1	2	3	4	5	6	7	8	9
Pre-treatments	Washing with 10 mins PBS and 20 mins UPW+CLO	----------							1 hour PBS washing
Conditions in the reactor	P=160 bar ; T=Below 40°C								
	t=1h	t=2h	t=1h 96% EtOH	t=2h 70% EtOH	t=1h	t=2h 70% EtOH	t=1h 96% EtOH	t=2h	
Treatments after the cycle	----------	5 cycles of freeze-thaw							----------
	Washing with UPW+CLO, following by washing with PBS								
Conditions during washing	Each run of washing: 10 mins direct sonication + Vortex + Oribital shaker								
Overnight condition	----------	Washing with PBS+CLO in orbital shaker	----------	Washing with PBS+CLO in orbital shaker	----------	Washing with PBS+CLO in orbital shaker	----------	Lyophilization	----------

Appendix F – Table band assignments of common biological molecules in the biological tissues.

Biomolecules	Peak position (cm^{-1})	Assignment
Collagen (Xu *et al.*, 2023; Salinas-Fernandez *et al.*, 2024; Jeevithan *et al.*, 2014; Li *et al.*, 2024)	3450 – 3300	**Amide A band** (N-H stretching)
	2950 – 2850	**Amide B band** (CH_2 asymmetric stretching)
	1700 – 1600	**Amide I band** (C=O stretching & hydrogen bond couple with COO^-)
	1550 – 1450	**Amide II band** (N-H bending & C-N stretching)
	1300 – 1180	**Amide III band** (N-H bending & C-N stretching)
GAGs (Brézillon, S. *et al.*, 2014)	1610 – 1410	**Uronic acid** (planar COO^- asymmetric and symmetric)
	1250 – 1220	SO_3^- **Sulfated GAGs**

			(S-O asymmetric vibration)
		1150 – 1100	**Ester linkage of the sulfated group** (C-O-S asymmetric stretching)
		1100 – 1000	**Structural backbone and glycosidic linkages** (C-O-C, C-C-C and C-C-O stretching)
		1000 – 980	**Carboxyl or amine-linked sulfate groups** (S=O symetric stretching)
Elastin (Popescu, M. C. et al., 2010)		3310 – 3315	**Amide A band** (N-H stretching vibrations)
		1656 – 1640	**Amide I band** (C=O stretching)
		1539 – 1530	**Amide II band** (N-H bending and C-N stretching)
		1350 – 1295	**Elastin backbone** (C-H symmetric and asymmetric bending)
		1266 - 1260	**Crosslinking regions in elastin** (C-O-C asymmetric stretching)
		1248 – 1236	**Amide III band** (N-H bending and C-N stretching)
		1170 – 1165	**Ester-linked carbonyl groups** (C=O stretching)
		966 – 952	**Hydrophobic domains** (C=C symmetric stretching)
Lipid (Lozano, M. *et al*., 2017; Pachetti, M. *et al.*, 2020; Frederick *et al.*, 2001)		3025 – 3005	C-H stretching
		2956 – 2925	CH_2 and CH_3 asymmetric stretching
		2870 – 2850	CH_2 and CH_3 symmetric stretching
		1750 – 1700	**Ester carbonyl groups** (C=O stretching)
		1475 – 1465	CH_2 bending
		1390 – 1375	CH_3 bending
		1250 – 1230	P=O asymmetric stretching
Genetic materials (Froehlich, E. *et al.*, 2011; Talari *et al.*, 2017; Mello *et al.*, 2012; Wood *et al.*, 2016)	**Guanine**	1716 – 1700	C=O stretching
		1699 – 1698	C_2=O stretching
		1528 – 1526	C=N stretching
		1373 – 1369	C-N stretching
		1604 – 1597	NH_2 vibration
	Cytosine	1665 – 1664	C=O stretching
		1656 – 1652	C_2=O stretching
		1576 – 1571	C=N stretching
		1373 – 1369	C-N stretching
	Thymine	1717 – 1706	C=O stretching
		1664 – 1661	C_2=O stretching
		1328 – 1327	C-N stretching
		1292 – 1288	N-H stretching

	Adenine	1604 – 1592	C=N stretching
		1328 – 1327	C-N streching
		1602 – 1601	N-H stretching
		1610 – 1600	C_7=N stretching
	Uracil	1665 – 1664	C=O stretching
		1637 – 1632	C=C stretching
		993 – 988	Ring bending
	Phosphate backbone	1260 – 1200	PO_2^- asymmetric stretching
		1100 – 1040	PO_2^- symmetric stretching
		970 – 965	O-P-O bending
		1100 – 1050	P-O-C asymmetric stretching
	Pentose sugar	1100 – 1000	C-O stretching
		1100 – 1030	C-OH stretching of oligosaccharides
		967 – 900	C-C and C-O skeletal vibrations
		899 – 890	Ring vibration
		968 – 834	Sugar-phosphate vibration